

## RESEARCH PAPER OPEN ACCESS

# Magnetic Resonance Cartography of Renal Tubule Volume Fraction During Diuretic Intervention

Ehsan Tasbihi<sup>1,2</sup>  | Thomas Gladysz<sup>1</sup>  | Jason M. Millward<sup>1,3</sup>  | Kathleen Cantow<sup>4</sup>  | Erdmann Seeliger<sup>4</sup>  | Thoralf Niendorf<sup>1,3</sup> 

<sup>1</sup>Max-Delbrück-Center for Molecular Medicine in the Helmholtz Association (MDC), Berlin Ultrahigh Field Facility (B.U.F.F.), Berlin, Germany | <sup>2</sup>Charité—Universitätsmedizin Berlin, Berlin, Germany | <sup>3</sup>Experimental and Clinical Research Center, A Joint Cooperation Between the Charité Medical Faculty and the Max Delbrück Center for Molecular Medicine, Berlin, Germany | <sup>4</sup>Institute of Translational Physiology, Charité—Universitätsmedizin Berlin, Berlin, Germany

**Correspondence:** Thoralf Niendorf ([thoralf.niendorf@mdc-berlin.de](mailto:thoralf.niendorf@mdc-berlin.de))

**Received:** 24 April 2025 | **Revised:** 7 July 2025 | **Accepted:** 12 August 2025

**Funding:** This work has been funded in part (TN) by the Deutsche Forschungsgemeinschaft (DFG, German Research Foundation)—project number/Projektnummer, NI 532/27-1.

**Keywords:** furosemide | kidney | MRI | tubule system | tubule volume fraction

## ABSTRACT

**Aim:** The renal tubular volume fraction (TVF) fluctuates under physiological conditions, and is altered in several renal diseases. Tools that enable noninvasive assessment of TVF are currently lacking. Magnetic Resonance (MR) TVF cartography is a novel approach for unraveling renal (patho-)physiology. Here, we employ MR-TVf cartography to monitor changes in response to the diuretic furosemide, and examine its role for the interpretation of renal oxygenation assessed by mapping the MRI relaxation time  $T_2^*$ . We hypothesize that furosemide increases TVF.

**Methods:** In anesthetized rats ( $n = 7$ ) the MRI relaxation times  $T_2$ ,  $T_2^*$ ,  $T_2'$  and kidney size were obtained before/after an i.v. bolus of furosemide using a 9.4 Tesla MRI scanner. Spectral analysis of the  $T_2$  signal decay was performed to estimate the number of  $T_2$  components in renal tissue. TVF cartographies were calculated using voxel-wise bi-exponential fit of the  $T_2$  decay. Near Infrared Spectroscopy (NIRS,  $n = 9$ ) was used to assess the total hemoglobin concentration (HbT) as a surrogate of renal blood volume.

**Results:** Furosemide induced changes in renal MRI and NIRS parameters relative to baseline:  $\text{TVF}_{\text{CORTX}} = 31.1\%$ ,  $\text{TVF}_{\text{OUTER\_MEDULLA}} = 30.7\%$ ,  $T_{2\text{-CORTX}} = 13.0\%$  and  $T_{2\text{-OUTER\_MEDULLA}} = 20.6\%$ .  $\text{HbT}_{\text{CORTX}}$  was reduced by 2.7%.  $\text{HbT}_{\text{MEDULLA}}$  declined by 8.6%. Kidney size showed a modest increase of 2.9%.  $T_{2\text{-OUTER\_MEDULLA}}^*$  and  $T_{2\text{-OUTER\_MEDULLA}}'$  rose by 20.5% and 20.2%.  $T_{2\text{-CORTX}}^*$  and  $T_{2\text{-CORTX}}'$  remained unchanged.  $T_2^*$  and TVF were strongly correlated in the outer medulla and moderately in the cortex.

**Conclusion:** MR-TVf cartography is highly relevant for elucidating mechanisms of renal (patho-)physiology, including the role of renal oxygenation assessed by MRI mapping of renal  $T_2^*$ .

## 1 | Introduction

The fluid volume within the renal tubules fluctuates significantly under physiological conditions and in various clinical scenarios and renal diseases. However, there is currently no

available noninvasive method to quantify or investigate the tubular fluid volume and its proportion to the total kidney volume—that is, the tubular volume fraction (TVF). Such a method is urgently needed, since the existing clinical diagnostic tools cannot detect changes in the TVF. The TVF is supposed to be

This is an open access article under the terms of the [Creative Commons Attribution](https://creativecommons.org/licenses/by/4.0/) License, which permits use, distribution and reproduction in any medium, provided the original work is properly cited.

© 2025 The Author(s). *Acta Physiologica* published by John Wiley & Sons Ltd on behalf of Scandinavian Physiological Society.

altered in response to changes in the glomerular filtration rate (GFR), tubular water reabsorption, the transmural pressure of the tubules, outflow of urine into the extrarenal urinary tract, and from rarefaction of the tubules.

Changes in GFR are expected to result in parallel changes in TVF. Pathophysiologically relevant decreases in GFR are caused by reduced effective filtration pressure or reduced hydraulic conductance of the glomerular filter in a variety of clinical scenarios [1–6]. Increases in GFR are typical for the early stages of diabetic kidney disease and for the remaining kidney following unilateral nephrectomy [7, 8].

Alterations in tubular water reabsorption will result in opposite changes of the TVF. Hyperglycaemia leads to reduced water reabsorption; this also happens upon administration of diuretics, particularly osmotic and loop diuretics [9–11]. Loop diuretics like furosemide are widely used in clinical practice to enhance urine flow rate and NaCl excretion. They inhibit the NKCC2 transporter in the thick ascending limb of the loop of Henle, which results in decreased water reabsorption in the nephron portions distal to the thick ascending limb [11]. Polycystic kidney disease is also characterized by a progressive increase in the TVF [12]. Administration of X-ray contrast media during transcatheter cardiac procedures increases tubular fluid viscosity, thereby reducing tubular fluid flow and increasing intratubular pressure, which results in circular distension of the tubules [13]. Conversely, intrarenal edema formation following acute events such as ischemia/reperfusion injury increases intrarenal pressure and may lead to compression of the tubules, since the renal capsule is relatively rigid [14, 15].

Obstructions anywhere in the extrarenal urinary tract that reduce urine outflow will lead to increased TVF. Such obstructions can occur during endourologic procedures and can be caused by kidney stones, tumors, scar tissue, hyperplasia of the prostate, and congenital malformations [14, 16, 17]. Renal fibrosis is the final stage of most progressive kidney diseases. It is induced following inflammation due to autoimmune diseases and inflammatory responses to AKI, and in chronic kidney diseases and diabetic kidney disease. Interstitial fibrosis is often associated with a loss of tubules [5, 18].

Diagnostic tools that enable direct, noninvasive detection of TVF changes are lacking. When TVF changes are induced by changes in GFR, these can be roughly estimated from GFR measurements. GFR can be measured by classical clearance techniques; however, routine clinical diagnostics still rely on the serum concentration of creatinine and/or cystatin C [19]. These surrogate parameters for GFR have notoriously low sensitivity and a rather sluggish response to acute drops in GFR [19]. Obstructions of the extrarenal urinary tract are clinically diagnosed by ultrasonographic or X-ray urography, yet these methods do not enable assessment of potential concomitant increases in the TVF [13, 20]. Renal core needle biopsies are used to assess fibrosis and edema, among other markers of kidney pathology [21]. However, biopsy specimens usually contain mostly cortical tissue and are limited by inherent drawbacks, including sampling bias and reliance on qualitative, subjective

clinical interpretation [21]. Moreover, biopsies are invasive, risking damage to an already compromised kidney and have a nonnegligible rate of complications [22].

Current state-of-the-art techniques for visualizing the tubular lumen with histology or intravital imaging using multiphoton microscopy require invasive procedures, making them entirely unfeasible for longitudinal preclinical studies or eventual clinical use. Intravital microscopy is typically restricted to superficial, localized regions of the kidney [23]. Magnetic Resonance Imaging (MRI) is a nondestructive technique that has proven invaluable for structural and functional nephrology [24–27]. Although the spatial resolution of MRI is on the mesoscopic scale, ranging from about 20  $\mu\text{m}$  (preclinical) to the millimeter range (clinical), it allows the study of cellular-level tissue microstructure and tissue water compartments. By utilizing the biophysics behind the MR transversal relaxation time  $T_2$ , MRI provides a window into the TVF.  $T_2$  cartography is a quantitative MRI approach used to generate a spatial map of  $T_2$  throughout a field of view. This method has been used to map the myelin water fraction in cerebral white matter in vivo [28, 29]. The water-containing compartments of renal tissue include (i) the intracellular space, (ii) the interstitial space, (iii) the lumen of the intrarenal vasculature with flowing blood, and (iv) the tubular lumen with flowing tubular fluid—a compartment unique to the kidney. In the kidney, the parenchyma and blood compartments exhibit similar  $T_2$  relaxation times. The tubular fluid has a considerably longer  $T_2$  relaxation time than the parenchyma and blood compartments. The contributions of the slow and fast  $T_2$  relaxation components to the  $T_2$  decay of the MR signal can be decomposed to provide useful information on the renal microstructure; the amplitude of the long  $T_2$  component is a surrogate of the TVF [30, 31].

Our recent work demonstrated proof-of-principle of dynamic mapping of the MRI relaxation time  $T_2$  for TVF cartography in rats [31]. This approach facilitated parametric mapping of TVF obtained in vivo under baseline conditions, and upon a clinically realistic acute intervention that increased renal pelvis and tubule pressure [31]. The TVF response to intravenous administration of furosemide has not been explored so far.

Seizing this opportunity, this study focuses on MR cartography to reveal alterations in the renal tubule volume fraction during a diuretic intervention using furosemide. In this work, we define TVF as the internal volume of the tubular lumen that varies with changes in the tubular fluid volume, not the total volume that includes the tubular epithelial cells. We hypothesize that furosemide increases the TVF in rat kidneys. To test this hypothesis, we conducted simultaneous assessment of the TVF derived from the  $T_2$  decay of the MR signal and of kidney size obtained from  $T_2$ -weighted MR images. In parallel, we performed spatially resolved quantification of the effective transversal relaxation time  $T_2^*$ , which is an MRI surrogate of renal oxygenation. We also examined the total hemoglobin concentration (HbT), which is a surrogate of the renal blood volume fraction, using near-infrared spectroscopy (NIRS). Changes in TVF, kidney size, and HbT were examined to explore confounding effects on MRI-based assessment of renal oxygenation.

## 2 | Results

### 2.1 | Spectral Analysis of the $T_2$ Relaxation of Renal Parenchyma and Tubular Fluid

To evaluate the decomposition of  $T_2$  relaxation into short and long  $T_2$  water fractions, we performed data-driven spectral analysis of the renal  $T_2$  decay using a free fit with nonnegative least squares (NNLS) approach. In vivo data were acquired from two rats ( $n = 2$ ) using a  $T_2$  mapping protocol with an extended echo time range (defined as long TE range protocol, Table 1). This approach was used to determine the number of water compartments, quantify the  $T_2$  relaxation time of rat

tubular fluid ( $T_{2\_long}$ ), and examine the short  $T_2$  relaxation time ( $T_{2\_short}$ ). Figure 1 shows a representative example of a  $T_2$  spectrum in a rat kidney for the renal cortex (CO), outer medulla (OM) and inner medulla (IM). The analysis of the  $T_2$  decay yielded two peaks, one peak representing the parenchyma and blood compartments, and the other peak representing the tubular fluid. The parenchyma and blood compartments showed a  $T_2$  distribution of  $T_{2\_short} = 10\text{--}40$  ms. The tubular fluid had a  $T_2$  distribution of  $T_{2\_long} = 80\text{--}220$  ms. The detection of the  $T_2$ -short peak is consistent with previous reports of  $T_2 \approx 40$  ms for arterial blood,  $T_2 \approx 41$  ms for the renal cortex, and  $T_2 \approx 52$  ms for the outer medulla at 9.4 T [32, 33]. Therefore, we ascribed the  $T_{2\_short}$  to parenchyma and renal blood. Prior studies have

**TABLE 1** | Synopsis of the parameters used for the MRI protocols deployed for  $T_2^*$ ,  $T_2$  mapping, and for kidney size estimation.

Method	$T_2$ mapping		$T_2^*$ mapping
	Long-TE range protocol	Short-TE range protocol	Multi gradient-echo
Repetition time TR (ms)	2000	Prospective triggering minimum was set to 500	50
Number of echoes	42	13	10
First echo time $TE_1$ (ms)	6.96	6.4	2.1
Inter-echo time $\Delta TE$ (ms)	6.96	6.4	2.1
Flip angle: $\alpha_{\text{refocusing pulse}}(^{\circ})$ or $\alpha_{\text{excitation}}(^{\circ})$	$180^{\circ}$	$180^{\circ}$	$16^{\circ}$
Number of averages NA	1	1	4
Acquisition time $t_{\text{acq}}$ (s)	170	58	23
In-plane spatial resolution w/o zero filling ( $\mu\text{m}^2$ )	$226 \times 445$	$226 \times 445$	$226 \times 445$
Field of view ( $\text{mm}^2$ )	$38.2 \times 50.3$	$38.2 \times 50.3$	$38.2 \times 50.3$
Matrix size	$169 \times 215$	$169 \times 215$	$169 \times 215$

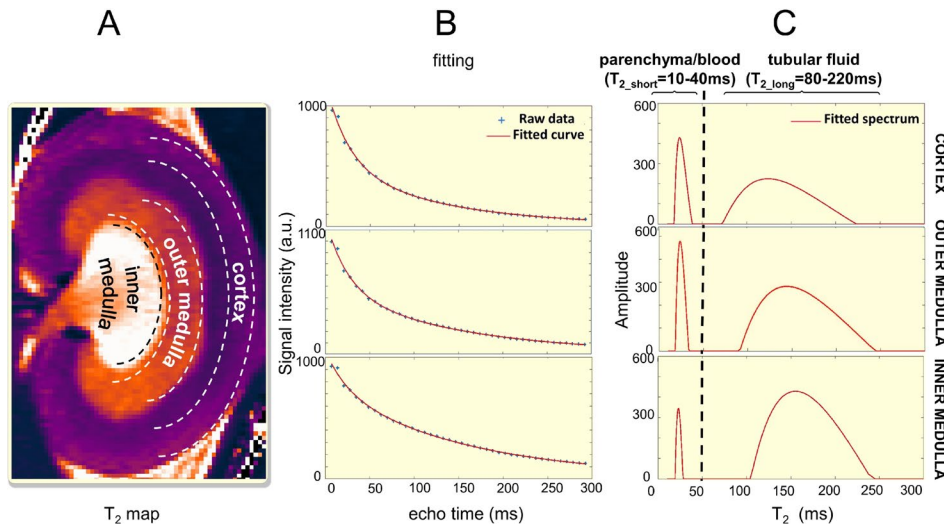


**FIGURE 1** | Spectral analysis of the relaxation time  $T_2$  using a free fit with the nonnegative least squares (NNLS) algorithm. (A) In vivo  $T_2$  map of a rat kidney. For spectral analysis of  $T_2$  relaxation regions of interest (ROI) were defined for the renal cortex, the outer medulla and the inner medulla. (B) Representative example of the  $T_2$  fitting for the regions of interest highlighted in A with NNLS. (C)  $T_2$  spectrum obtained for a rat kidney using the ROIs highlighted in A. For data acquisition a minimum echo time of  $TE = 6.96$  ms ( $\Delta TE = 6.96$  ms, number of echoes = 42 TR = 2000 ms) was used.

reported a  $T_2$  value of approximately 180 ms for mouse urine at 9.4 T [34], however, there are no published reports on  $T_2$  relaxation times of rat tubular fluid at 9.4 T. To close this gap and further validate the results obtained from the spectral analysis of the  $T_2$  decay, we measured  $T_2 = 150 \pm 45$  ms of rat urine collected from the bladder at body temperature  $T = 37^\circ\text{C}$  ( $n = 2$ ,  $\text{pH} = 6.0$ ). This finding is in accordance with the second peak obtained from the spectral analysis and is within this peak's  $T_2$  distribution of  $T_{2\_long} = 80\text{--}220$  ms, and hence represents the tubular fluid. Assuming that substances typically present in the tubular fluid of healthy subjects do not substantially influence  $T_{2\_long}$  [33], the relaxation time is expected to remain relatively constant across different renal layers. Accordingly, for in vivo TVF assessment, the value of  $T_{2\_long} = 150$  ms was fixed as the long component of a bi-exponential nonlinear fit of the  $T_2$ -relaxation driven MR signal decay in the short TE range protocol.  $T_{2\_short}$  was constrained between 10 ms and 40 ms.

## 2.2 | Validation of TVF Assessment in Phantom Study

Validation of TVF assessment including absolute TVF values was done using a phantom containing rat urine with known volume fractions. Figure 2A shows a  $T_2$  map obtained for the phantom. The inner tube of the left phantom (ROI1) has a  $T_2$  distribution of 58–69 ms, mimicking the  $T_2$  relaxation times of the renal blood/parenchyma. The inner tube of the right phantom (ROI2) has a  $T_2$  distribution of 180–260 ms, mimicking the  $T_2$  relaxation time of tubular fluid. A single MRI voxel in the kidney can contain multiple, isolated water compartments. We simulated this by assuming the summation of the signals measured in the ROI1 and ROI2 in Figure 2A arises from the same voxel. The two ROIs contain nearly identical volumes of water, so the proton populations should be nearly identical, and the true relative fractions (ground truth) should be  $\approx 50\%$ . Similarly, by scaling the signal measured from the left and right ROI, we can simulate the tubule water fraction for different ranges.

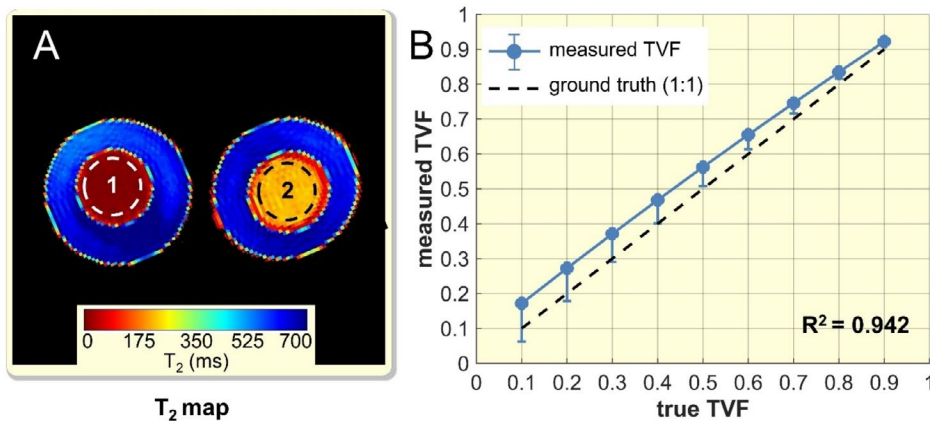


**FIGURE 2** | Evaluation of absolute TVF values in a phantom study: (A)  $T_2$  map in milliseconds of the phantom scanned with the short TE protocol using multi-echo spin-echo ( $\text{TR} = 500$  ms, number of echoes = 13, first  $\text{TE} = 6.4$  ms, inter-echo time  $\Delta\text{TE} = 6.4$  ms, number of averages = 1,  $\alpha_{\text{refocusing pulse}} = 180^\circ$ ,  $t_{\text{acquisition}} = 58$  s) with selected region-of-interest (ROI1–ROI2). ROI1 has a  $T_2$  distribution similar to the  $T_2$  bandwidth of blood/parenchyma. ROI2 has a  $T_2$  distribution similar to the  $T_2$  bandwidth of tubular fluid. The outer tubes are filled with distilled water used as a reference. (B) Evaluation of the assessment of the absolute volume fraction with decomposition of parametric  $T_2$  using bi exponential fitting of the  $T_2$  decay with fixed  $T_{2\_long}$ . The coefficient of determination  $R^2$  of 0.942 indicates a strong agreement for TVF assessments.

Figure 2B shows absolute TVF estimated with a bi-exponential fit ( $T_{2\_short}$  lower band = 50 ms— $T_{2\_short}$  upper band = 80 ms.  $T_{2\_long}$  fixed = 220 ms). For the TVF assessment, a mean absolute error (MAE) of  $5.6\% \pm 1.8\%$  and an adjusted  $R^2$  of 0.942 were observed.

## 2.3 | Validation of TVF Assessment With Synthetic Data

We simulated  $T_2$  decays to examine the accuracy of our bi-exponential fit with a fixed  $T_{2\_long}$  on the TVF assessment. Table 2 summarizes the impact of fixing  $T_{2\_long}$  at 150 ms on the assessment of absolute TVF and relative changes in TVF. Relative changes refer to the difference in TVF between two consecutive points ( $n$ ,  $n-1$ ), expressed as a percentage of the value of the previous point. Since the relative changes remain fairly similar to ground truth across a wide range of TVFs, the error in the relative changes is sufficiently small despite the inherent bias in the absolute TVF values (Table 2).

## 2.4 | Tubular Volume Fraction Changes Upon Furosemide Application

Representative TVF maps were derived from bi-exponential decomposition of  $T_2$  decays obtained from rats in vivo (Figure 3, left). Data was acquired during baseline, and during the first interval (1–10 min) after intravenous bolus injection of furosemide followed by a saline chaser (to ensure that the entire furosemide dose entered the circulation). Data was then acquired during a second interval (12–20 min), when a balanced electrolyte solution (Ringer's solution) was continuously infused to replace the volume and electrolyte loss caused by furosemide. Under baseline conditions, TVF values were  $\text{TVF}_{\text{CORTEX}} = 29.8\% \pm 2.2\%$  (mean  $\pm$  SEM,  $n = 7$ ),  $\text{TVF}_{\text{OUTER\_MEDULLA}} = 42.6\% \pm 2.9\%$ , and  $\text{TVF}_{\text{INNER\_MEDULLA}} = 76.4\% \pm 3.7\%$ . Figure 4A shows the time courses of relative changes in TVF in response to furosemide and the subsequent infusion of Ringer's solution. TVF changes were

**TABLE 2** | Representative mean absolute error (MAE) for TVF relative changes, which were derived from analysis of the simulated  $T_2$  decays using bi-exponential fitting, covering a broad physiological range of TVFs. During the fitting process, (left column)  $T_{2\_long}$  was incorrectly fixed at 150 ms, which is shorter than its actual simulated value of 200 ms. (center column)  $T_{2\_long}$  was correctly fixed at 150 ms, which is equal to its actual simulated value of 150 ms. (right column)  $T_{2\_long}$  was incorrectly fixed at 150 ms, which is longer than its actual simulated value of 100 ms. Other parameters of the simulation are identical with those used for TVF assessment in vivo MRI study first TE = 6.4 ms, inter-echo time  $\Delta TE = 6.4$  ms, number of echoes = 13,  $\alpha_{refocusing\_pulse} = 170^\circ$  (to account for imperfect refocusing pulses).

$T_{2\_long}$ incorrect fixation (underestimated)				$T_{2\_long}$ correct fixation				$T_{2\_long}$ incorrect fixation (overestimated)			
Ground truth simulated with $T_{2\_long} = 200$ ms				Ground truth simulated with $T_{2\_long} = 150$ ms				Ground truth simulated with $T_{2\_long} = 100$ ms			
$T_{2\_long}$ set to 150 ms during fitting				$T_{2\_long}$ set to 150 ms during fitting				$T_{2\_long}$ set to 150 ms during fitting			
Ground truth											
TVF relative change (%)				MAE for relative change (%)				MAE for relative change (%)			
TVF (%)	TVF (%)	TVF relative change (%)	MAE for relative change (%)	TVF (%)	TVF (%)	TVF relative change (%)	MAE for relative change (%)	TVF (%)	TVF (%)	TVF relative change (%)	MAE for relative change (%)
$n$											
1	20.0	33.3	23.9±0.6	34.3	2.0	21.6±1.3	30.1	5.0	12.8±0.8	34.7	4.7
2	25.0	25.0	29.9±0.6	25.1	1.6	26.6±1.3	23.1	4.2	16.0±0.8	25.0	4.2
3	30.0	20.0	35.9±0.5	20.1	1.3	31.5±1.3	18.4	3.6	19.2±0.9	20.0	3.9
4	35.0	16.7	41.9±0.5	16.7	1.1	36.5±1.3	15.9	3.1	22.4±0.9	16.7	3.6
5	40.0	14.3	47.8±0.5	14.1	0.9	41.5±1.3	13.7	2.8	25.5±1.0	13.8	3.5
6	45.0	12.5	53.6±0.5	12.1	0.8	46.4±1.3	11.8	2.5	28.5±1.0	11.8	3.5
7	50.0	11.1	59.4±0.5	10.8	0.8	51.4±1.2	10.8	2.3	31.5±1.1	10.5	3.6
8	55.0	10.0	65.2±0.5	9.8	0.9	56.4±1.2	9.7	2.1	34.3±1.3	8.9	3.8
9	60.0	9.1	70.8±0.5	8.6	0.9	61.3±1.2	8.7	1.9	37.0±1.4	7.9	4.2
10	65.0	8.3	76.4±0.6	7.9	0.8	66.3±1.1	8.2	1.7	39.5±1.6	6.8	4.7
11	70.0	7.7	82.1±0.5	7.5	0.7	71.2±1.1	7.4	1.5	41.8±1.8	5.8	4.9
12	75.0	7.1	87.7±0.5	6.8	0.6	76.1±1.1	6.9	1.4	44.0±1.7	5.3	3.8
13	80.0	6.7	93.5±0.5	6.6	1.5	81.0±1.0	6.4	1.3	46.9±1.3	6.6	3.2

Note: The bold values in Table 2 are ground truth and predefined simulation parameters and therefore contain no error.

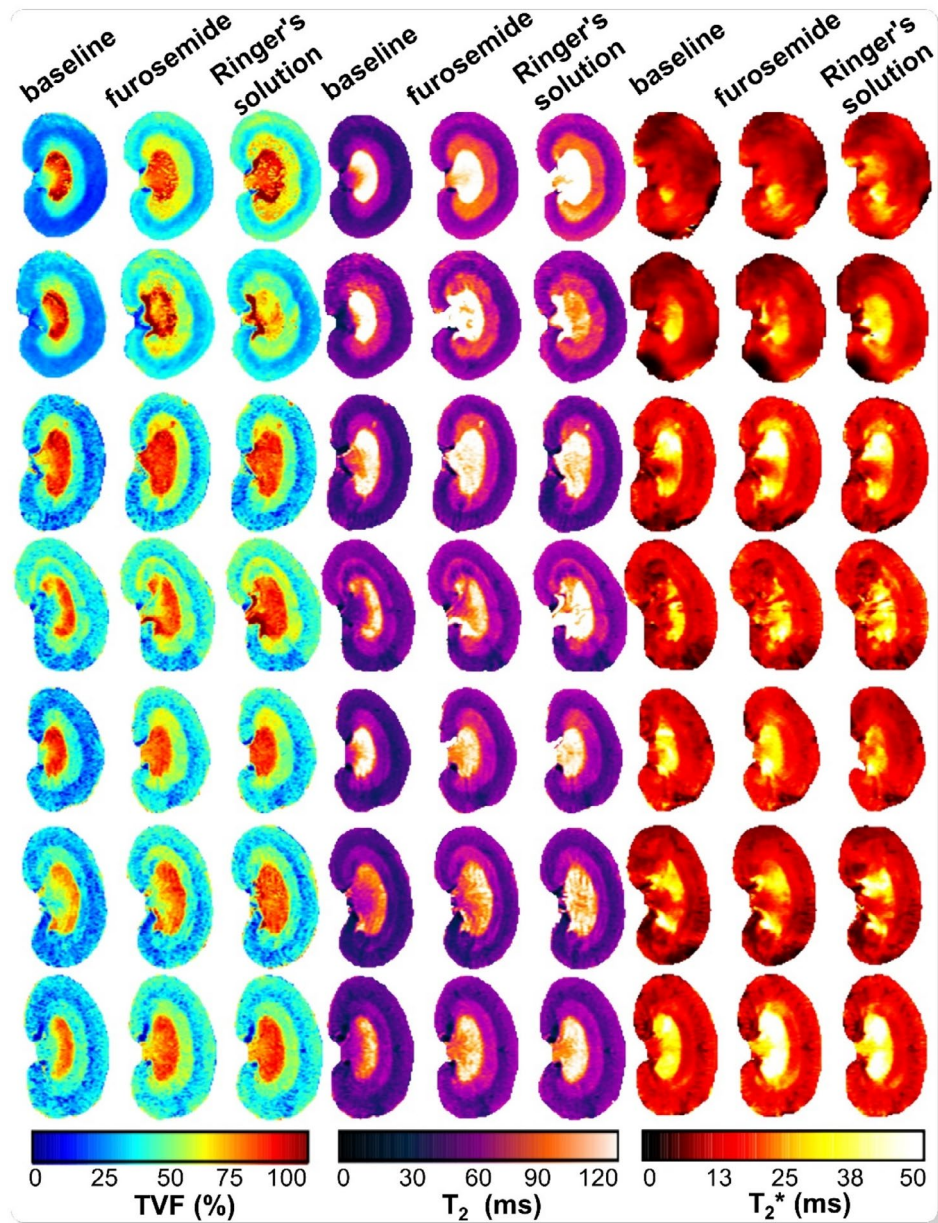


**FIGURE 3** | Cartography of the tubular volume fraction TVF and the MR relaxation times  $T_2$  and  $T_2^*$  obtained in rat kidneys in vivo at baseline, ~4 min after furosemide injection, and ~18 min after furosemide injection ~6 min after the start of the infusion of the electrolyte solution (Ringer's solution). Marked alterations in TVF and  $T_2$  following furosemide injection are visually evident. Postinjection, an increase in TVF was observed in both the renal cortex and outer medulla. Similarly,  $T_2$  values exhibited a notable rise in the renal cortex and outer medulla. Additionally, a marked increase in  $T_2^*$  was observed in the outer medulla.

immediately observed after furosemide injection. Averaged over the four time points of the first time interval,  $\text{TVF}_{\text{CORTEX}}$  increased by  $31.1\% \pm 6.3\%$  compared to baseline. Averaged over the three time points of the second time interval,  $\text{TVF}_{\text{CORTEX}}$  remained increased by  $33.8\% \pm 5.7\%$  vs. baseline. A similar effect was observed in the OM, where TVF increased by  $30.7\% \pm 6.2\%$  during the first interval and remained increased by  $34.8\% \pm 5.6\%$  during the second interval. In the IM, our data suggest a slight increase of TVF by  $8.8\% \pm 3.8\%$  in the first interval and by  $11.7\% \pm 4.4\%$  in the second interval, although these results were not statistically significant.

Statistical analyses by ANOVA documented significant changes in TVF. Pair-wise comparisons showed that  $\text{TVF}_{\text{CORTEX}}$  was significantly increased versus baseline during the first interval ( $p=0.0075$ ,

Figure 5) and remained significantly higher than baseline during the second interval ( $p=0.0033$ ). Pair-wise comparison of  $\text{TVF}_{\text{OUTER\_MEDULLA}}$  showed a significant increase between baseline and the first interval ( $p=0.0325$ , Figure 6) and the second interval ( $p=0.0005$ ). The pair-wise comparisons of  $\text{TVF}_{\text{INNER\_MEDULLA}}$  did not show significant changes between baseline and the first interval ( $p=0.5443$ ) or the second interval ( $p=0.1841$ ).

## 2.5 | $T_2^*$ Changes Upon Furosemide Application

For MRI-based assessment of renal oxygenation, quantitative in vivo  $T_2^*$  maps were generated during baseline, after furosemide application followed by the saline chaser (1–10 min),

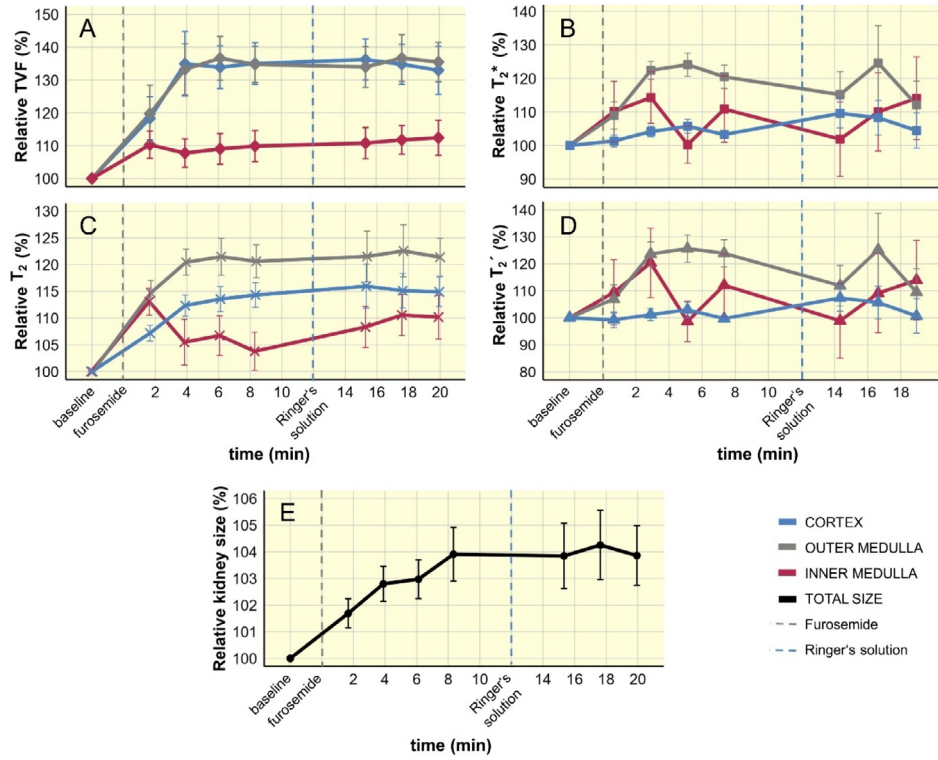


**FIGURE 4** | Time courses of relative changes following administration of furosemide. (A) Time course of TVF changes (mean  $\pm$  SEM,  $n = 7$ ) for cortex (blue), outer medulla (gray), inner medulla (red) before the intervention (baseline), after the furosemide administration (gray dashed line) and during the infusion of Ringer's solution (blue dashed line), (B) time course of  $T_2^*$  changes for cortex, outer medulla, inner medulla, (C) time course of  $T_2$  changes for cortex, outer medulla, inner medulla, (D) time course of  $T_2'$  changes for cortex, outer medulla, inner medulla, and (E) time course of kidney size changes before (baseline) and during these interventions. Gray dashed line at time = 0 indicates the start of the furosemide injection. Blue dashed line at time = 12 min indicates the start of the infusion of the electrolyte solution (Ringer's solution). Time points at  $t = 2$  min, 4 min and 6 min are reported as mean  $\pm$  SEM of  $n = 6$  rats. This is due to the different time point of acquisition in the first two rats, which underwent MR scans using both the long TE range and short TE range protocols.

and the second interval (12–20 min) during the infusion of the balanced electrolyte solution (Figure 3, right). Under baseline conditions,  $T_2^*$  CORTEX was  $11.9 \pm 0.7$  ms,  $T_2^*$  OUTER\_MEDULLA  $12.3 \pm 0.5$  ms, and  $T_2^*$  INNER\_MEDULLA  $22.0 \pm 3.0$  ms ( $n = 7$ ). The  $T_2^*$  time course is shown in Figure 4B. Furosemide led to a significant  $T_2^*$  increase in the OM by  $20.5\% \pm 3.9\%$  ( $p = 0.0075$ ) during the first interval (averaged over 4 time points) and remained increased by  $19.2\% \pm 7.4\%$  ( $p = 0.0325$ ) in the second interval (averaged over 3 time points), but not in CO or IM (Figure 5). Changes in  $T_2^*$  OUTER\_MEDULLA correlated strongly with changes in  $\text{TVF}_{\text{OUTER_MEDULLA}}$  ( $r = 0.81$ ), while  $T_2^*$  CORTEX showed moderate correlations with  $\text{TVF}_{\text{CORTEX}}$  ( $r = 0.5$ ; Figure 6).

## 2.6 | $T_2$ Changes Upon Furosemide Application

Quantitative  $T_2$  relaxation maps were derived from mono-exponential fits (Figure 3, center). Under baseline conditions,  $T_2$  was  $44.1 \pm 1.3$  ms for CO,  $53.3 \pm 1.5$  ms for OM, and  $103.6 \pm 4.8$  ms for IM ( $n = 7$ ). The  $T_2$  time course is presented in Figure 4C. After furosemide injection,  $T_{2\text{CORTEX}}$  increased by  $13.0\% \pm 2.3\%$  during the first interval (averaged over 4 time points) and remained increased by  $16.1\% \pm 3.6\%$  in the second interval (averaged over 3 time points).  $T_{2\text{OUTER_MEDULLA}}$  increased by  $20.6\% \pm 2.7\%$  in the first interval and remained increased by  $22.7\% \pm 4.5\%$  in the second time interval.  $T_{2\text{INNER_MEDULLA}}$  responses were inconsistent.

Statistical analysis showed significant  $T_2$  changes in response to furosemide for CO ( $p = 0.0012$ ) and OM ( $p = 0.0027$ ), but not for IM ( $p = 0.0515$ ) (Figure 5).  $T_2$  changes in CO and OM strongly correlated with changes in  $\text{TVF}_{\text{CORTEX}}$  and  $\text{TVF}_{\text{OUTER_MEDULLA}}$  ( $r = 0.92$ );  $T_{2\text{CORTEX}}$  showed moderate correlation with  $T_2^*$  CORTEX ( $r = 0.53$ ).  $T_{2\text{OUTER_MEDULLA}}$  showed strong correlation with  $T_2^*$  OUTER\_MEDULLA ( $r = 0.75$ ; Figure 6).

## 2.7 | $T_2'$ Changes Upon Furosemide Application

Under baseline conditions,  $T_2'$  was  $17.7 \pm 1.4$  ms for CO,  $17.8 \pm 1.3$  ms for OM, and  $18.3 \pm 1.0$  ms for IM ( $n = 7$ ). The  $T_2'$  time course is presented in Figure 4D. Furosemide only led to a significant  $T_2'$  increase in the OM by  $20.2\% \pm 3.6\%$  ( $p = 0.0272$ ) during the first interval (averaged over 4 time points) (Figure 5). Changes in  $T_2'$  correlated strongly with changes in  $T_2^*$  in CO, OM, and IM ( $r = 0.88, 0.99$ , and  $0.94$ , respectively; Figure 6).

## 2.8 | Kidney Size Changes Upon Furosemide Application

Kidney size (KS) showed significant changes in response to the furosemide intervention (Figure 4F). During baseline, the KS was  $201 \pm 17.4 \text{ mm}^2$  (mean  $\pm$  SEM,  $n = 7$ ). After

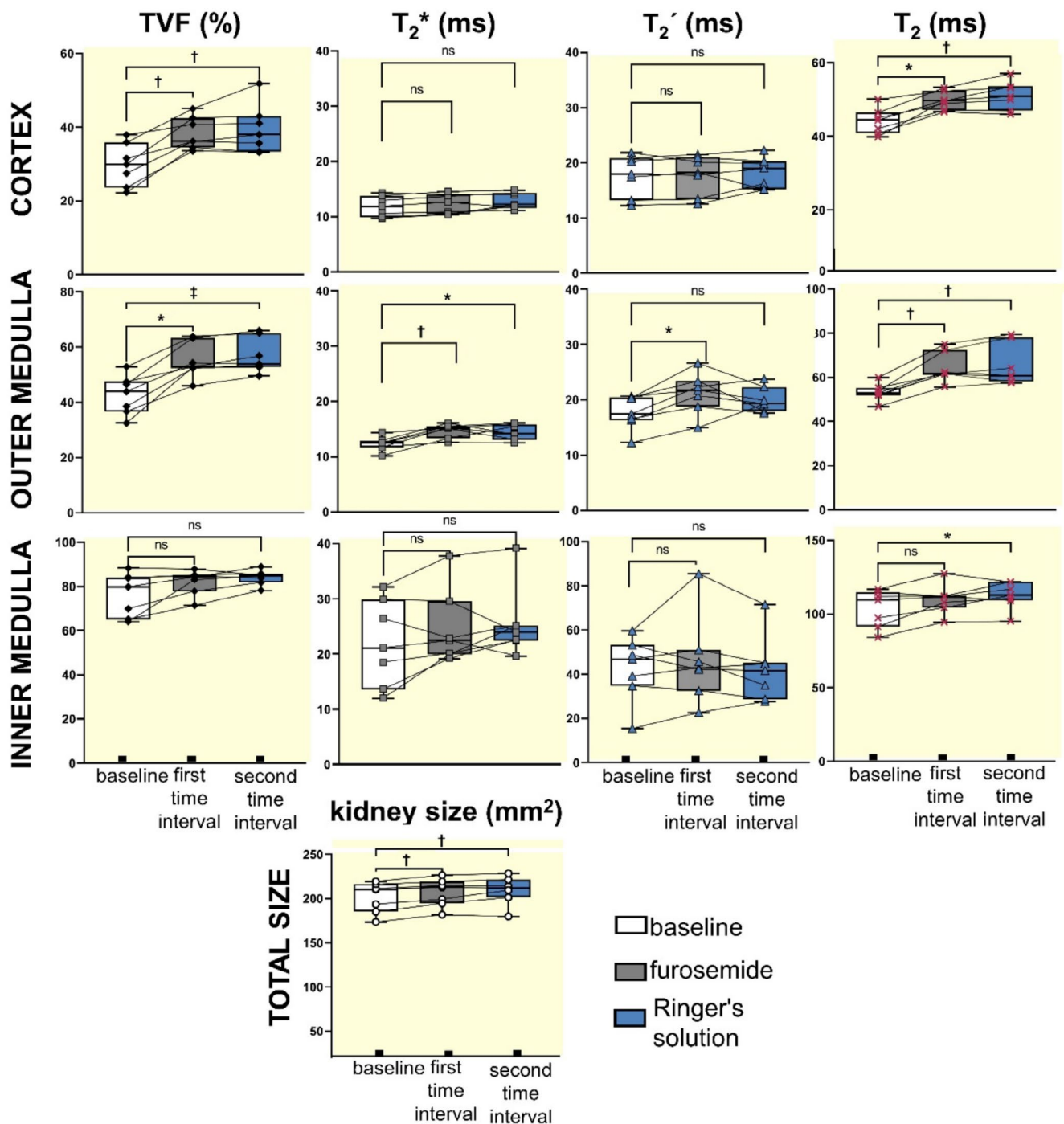


**FIGURE 5** | Changes in TVF,  $T_2^*$ ,  $T_2'$ ,  $T_2$  and kidney size following administration of furosemide. The TVF showed significant changes in response to furosemide in the renal cortex and outer medulla, but not in the inner medulla. Pair-wise comparisons show significant increases compared to baseline during the furosemide intervention and the Ringer's solution administration in the cortex ( $p=0.0075$ ,  $p=0.0033$ , respectively) and outer medulla ( $p=0.0325$ ,  $p=0.0005$ ).  $T_2^*$  was significantly increased in the outer medulla during the furosemide intervention and Ringer's solution administration ( $p=0.0075$ ,  $p=0.0325$ ).  $T_2^*$  changes were not significantly changed in the renal cortex and inner medulla.  $T_2'$  was significantly increased only in the outer medulla during the furosemide intervention ( $p=0.0272$ ).  $T_2$  was significantly increased during the furosemide intervention and Ringer's solution administration in the cortex ( $p=0.0162$ ,  $p=0.0013$ ) and outer medulla ( $p=0.0075$ ,  $p=0.0033$ ). In the inner medulla,  $T_2$  was significantly increased only during the Ringer's solution administration ( $p=0.0162$ ). Kidney size significantly increased during the intervention and upon Ringer's solution administration ( $p=0.0075$ ,  $p=0.0033$ ). Nonparametric repeated-measures Friedman test, with Dunn's post hoc test for pair-wise comparisons;  $n=7$ ; \* $p<0.05$ , † $p<0.01$ , ‡ $p<0.001$ .

furosemide injection, KS increased by  $2.9 \pm 0.6\%$  during the first interval (averaged over 4 time points) and remained increased by  $4.2 \pm 1.2\%$  in the second interval (averaged over

3 time points). Pair-wise comparisons revealed a significant increase in KS between baseline and the first time interval ( $p=0.0075$ ) and remained significantly increased during the

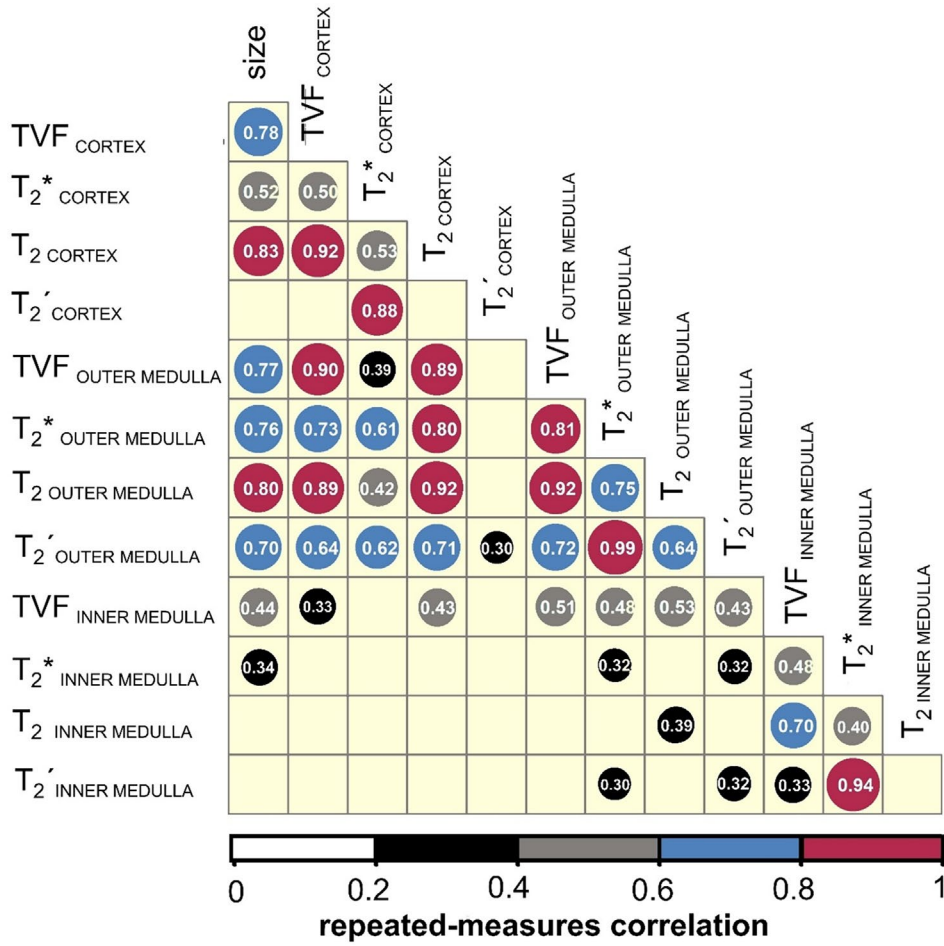


**FIGURE 6** | Repeated-measures correlation matrix illustrating the association between changes in TVF, kidney size,  $T_2^*$ ,  $T_2'$ ,  $T_2$  for the renal cortex, the outer medulla and the inner medulla. The color legend and the circle size indicate the strength of the correlation. Numbers inside circles indicate correlation coefficients;  $n=7$ . Nonsignificant correlations are omitted.

second interval ( $p=0.0033$ ) (Figure 5). KS changes correlated strongly with changes in  $T_2$  CORTEX and  $T_2$  OUTER MEDULLA ( $r=0.83$  and  $0.80$ , respectively). KS changes correlated strongly with changes in TVF CORTEX and TVF OUTER MEDULLA ( $r=0.78$  and  $0.77$ , respectively). KS changes showed moderate correlation with  $T_2^*$  CORTEX ( $r=0.52$ ) and a strong correlation with  $T_2^*$  OUTER MEDULLA ( $r=0.76$ ; Figure 6).

## 2.9 | Total Hemoglobin Concentration Changes Upon Furosemide Application

Near Infrared Spectroscopy (NIRS) was performed to assess changes in the total hemoglobin concentration, a surrogate of renal blood volume, upon furosemide application. Representative time courses showing relative changes in cortical and medullary total hemoglobin concentration (HbT) in response to intravenous furosemide administration in rats ( $n=9$ ) are presented in Figure 7. In the cortex, furosemide induced a modest but consistent decrease in HbT, with an average reduction of  $2.7\% \pm 0.1\%$  postinjection ( $p<0.0001$ ). In the medulla, HbT declined more prominently, with an average reduction of  $8.6\% \pm 0.1\%$  following furosemide administration. This was followed by a sustained plateau phase and remained significantly below baseline throughout the entire observation period of

12 min. Pairwise comparisons revealed a significant decrease in HbT between baseline and post furosemide administration ( $p<0.0001$ ). The reduction in HbT is indicative of a reduction in the renal blood volume fraction related to the concomitant TVF increase.

## 3 | Discussion

In this study, we applied bi-exponential analysis of the MRI  $T_2$ -decay to report for the first time in vivo changes of the tubular fluid volume fraction within the rat kidney in response to furosemide. Our approach adds an innovative physiometabolic dimension to imaging and provides a technical foundation and springboard for research into physiological and pathophysiological conditions of the renal tubular system. Due to the noninvasive nature, MR cartography of the TVF facilitates longitudinal studies and swift translation from preclinical research to human studies and clinical application.

We employed a novel approach and applied spectral analysis of the renal  $T_2$  relaxation decay in vivo. This analysis was conducted to determine the number of water compartments in the kidney and to assess the  $T_2$  relaxation times of rat tubular fluid and of the short  $T_2$  component. Detection of the  $T_{2\_short}$  peak

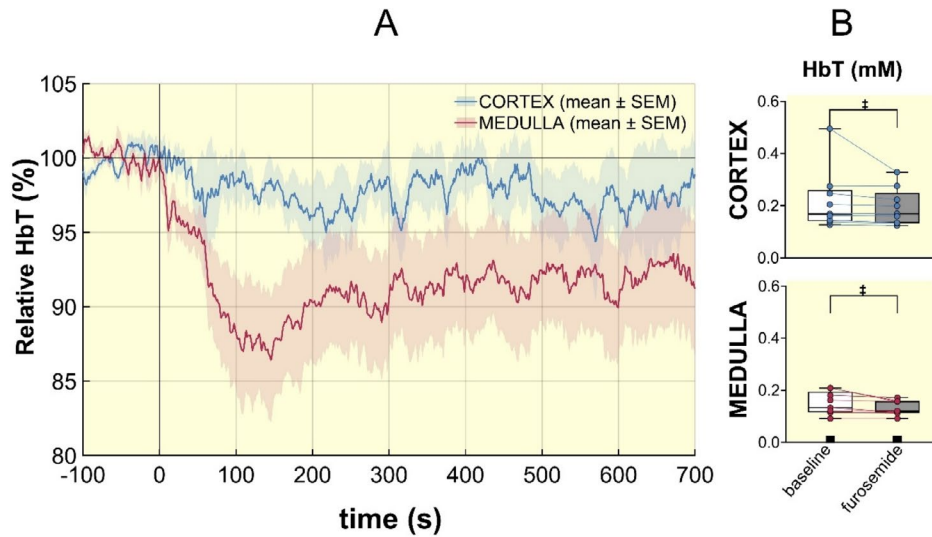


**FIGURE 7** | Changes in total hemoglobin concentration (HbT), a surrogate of renal blood volume fraction, obtained from near infrared spectroscopy (NIRS) in the renal cortex (blue) and medulla (red) following furosemide injection ( $n=9$ ). (A) Time course of relative HbT values are shown as percentage change relative to baseline. The vertical line indicates the time point of furosemide administration ( $t=0$ s). Shaded areas represent the standard error of the mean (SEM). (B) Furosemide administration led to a significant decrease from baseline in the cortex and medulla ( $p<0.0001$ ), assessed using a paired nonparametric Friedman test.

derived from the spectral analysis aligns with previous 9.4 T findings using mono-exponential fitting:  $T_{2\text{ ARTERIAL BLOOD}}\approx 40$  ms,  $T_{2\text{ CORTEX}}\approx 41$  ms, and  $T_{2\text{ OUTER MEDULLA}}\approx 52$  ms [32, 35, 36]. We therefore attributed  $T_{2\text{ short}}$  to the renal parenchyma and blood. While mouse urine  $T_2$  at 9.4 T has been reported [34], data for rat tubular fluid were lacking. To address this, we measured  $T_2$  in rat urine, which is consistent with the  $T_{2\text{ long}}$  peak derived from the spectral analysis, supporting its assignment to tubular fluid. Validation of the absolute TVF values was done using a phantom containing rat urine and material mimicking the relaxation properties of renal tissue with known volume fractions. The coefficient of determination  $R^2$  of 0.942 indicates a strong agreement for TVF assessments. Additionally, we conducted simulations to explore potential errors in TVF assessment that could arise from using short TE range protocols and fixation of the  $T_{2\text{ long}}$  value. The simulation results indicated that if  $T_{2\text{ long}}$  is fixed to an incorrect value, either below or above the true value, the absolute TVF could be misestimated. However, the relative changes in TVF remained consistent and predictable.

To investigate the effects of furosemide induced TVF changes in the rat kidney, we administered an intravenous bolus directly while the rats were in the MRI scanner. Furosemide inhibits the NKCC2 transporter in the thick ascending limb of the loop of Henle, which results in decreased water reabsorption in the nephron portions distal to the thick ascending limb. Our findings on TVF dynamics reflect this effect. We noted a significant TVF increase in the renal cortex ( $\text{TVF}_{\text{CORTEX}}$ ) and the outer medulla ( $\text{TVF}_{\text{OUTER MEDULLA}}$ ). A slight increase in the inner medulla was not statistically significant ( $\text{TVF}_{\text{INNER MEDULLA}}$ ). We demonstrated this method can be used to quantify acute dynamic changes in TVF. Therefore, MR-TVf cartography can be a valuable tool to investigate the mechanisms and assess the severity of certain renal diseases, particularly in the context of acute changes in TVF.

By inhibiting energy-dependent electrolyte reabsorption, furosemide reduces oxygen consumption in the thick ascending limb of the loop of Henle, which in turn elevates tissue oxygen levels, particularly in the OM. This was reflected by our observation of increases in the MRI relaxation times  $T_2^*$  and  $T_2$ , which are both surrogates of blood oxygenation [27]. While our current observations of  $T_2^*$  and  $T_2$  align with prior studies, the observed increases in  $T_2^*$ ,  $T_2$  are not solely due to improved oxygenation, as has hitherto generally been supposed [37–45]. The markedly more pronounced increase in TVF compared to the increase in kidney size is indicative of an increase in intrarenal pressure. Substantial increases in intratubular pressure following the administration of furosemide as well as another diuretic, acetazolamide, in rats have previously been reported [46–48]. Because the renal capsule is relatively rigid, intrarenal pressure will increase. This results in intrarenal compartment syndrome: intrarenal blood vessels become compressed and the renal blood volume fraction (BVF) is therefore reduced when the intrarenal pressure increases [14, 15]. Our findings derived from NIRS demonstrate furosemide-induced reduction in the BVF: the concentration of total hemoglobin per tissue volume, a surrogate parameter for BVF, was markedly decreased, especially in the renal medulla.

We observed an increase in TVF in response to furosemide administration. This change was similar for the renal cortex and outer medulla. The  $T_2^*$  increase in the cortex was much smaller than in the outer medulla. This observation is consistent with results obtained in healthy subjects: furosemide injection resulted in about a 50% increase in medullary  $T_2^*$ , while cortical  $T_2^*$  was barely changed [37, 49]. Four effects contribute to this phenomenon. First, a considerable portion of the cortical vessels are arteries, arterioles, and veins, and their vessel walls will withstand the compression better than the comparatively supple walls of the microvessels in the medulla. Second, the average oxygen saturation of the hemoglobin in the cortical vessels is typically

higher than in the medulla [50], leading to a weaker deoxyhemoglobin reduction even if the blood volume fraction reduction was similar. Third, the absolute value of the tubular volume fraction is smaller in the cortex. This means a similar relative change relates to a smaller absolute change. Fourth, changes in the total hemoglobin concentration (HbT), a surrogate of the BVF, were much more pronounced in the medulla than in the renal cortex, as demonstrated by our NIRS measurements.

The MRI relaxation times  $T_2$  and  $T_2^*$  are sensitive to the concentration of deoxyhemoglobin (deoxyHb) per tissue volume, so any reduction in BVF increases  $T_2$  and  $T_2^*$  [27]. Therefore,  $T_2^*$ ,  $T_2$  based assessments of furosemide-induced changes in renal oxygenation overestimate the gain in true tissue oxygenation, that is, in the tissue partial pressure of oxygen ( $pO_2$ ). An early study in rats that utilized invasive probes—the “gold standard” for measuring true tissue oxygenation—reported an increase in medullary  $pO_2$  upon a large bolus dose of furosemide, while cortical  $pO_2$  remained unchanged [50]. In order to determine the contribution of the true oxygenation gain versus the effects of the compartment syndrome-induced changes, concurrent  $T_2$  and  $T_2^*$ -based evaluations of tissue oxygenation coupled with measurements from invasive probes are necessary.

It has long been recognized that changes in kidney size are indicative of certain pathophysiological developments. An increasing body of literature outlines the potential of noninvasive imaging for evaluating kidney size as a clinical parameter in the diagnosis, treatment monitoring, and prognosis in renal disease [51]. A notable example is polycystic kidney disease (PKD), wherein kidney size correlates with disease progression [12, 52, 53]. Consequently, the U.S. Food and Drug Administration and the European Medicines Agency now include kidney size as a prognostic marker for use in clinical trials of new therapies for autosomal dominant PKD [54, 55]. Detecting reduction in kidney size due to parenchymal atrophy, sclerosis, and fibrosis has also been recognized as a tool to identify chronic kidney disease and to determine its severity [56, 57]. Imaging-based kidney size is currently included as a prognostic imaging marker for diabetic kidney disease [58], and was recently proposed for longitudinal monitoring for several renal diseases including hyperfiltration in early diabetic nephropathy, renal transplants, renal artery stenosis, and vesicoureteral reflux [59]. Preclinical MRI studies emulating various clinical conditions and acute scenarios have documented substantial changes in kidney size. This included clinically relevant scenarios with primary changes in TVF, in BVF, or in both fractions [31, 60–71]. The results of the current study corroborate that a furosemide-induced TVF increase is sufficient to result in a small increase in kidney size.

Renal tissue hypoxia is a pivotal early element in the pathophysiology of acute kidney injury and its subsequent progression to chronic kidney disease. Hypoxia also plays a major role in the pathophysiology of diabetic kidney disease [70, 72–77]. Therefore, assessment of renal oxygenation by  $T_2^*$  and  $T_2$  MRI could become a vital assay for research into renal (patho-)physiology and for clinical application. However, as these metrics reflect the amount of deoxyHb per tissue volume,  $T_2^*$  and  $T_2$  are also dependent on the renal BVF. One cause for changes in renal deoxyHb independent of changes in blood oxygenation is alterations in TVF, because changes in TVF likely induce alterations

in renal BVF. Indeed, TVF is recognized as a major confounding factor influencing the relationship between renal  $T_2^*$  and  $T_2$  and tissue  $pO_2$  [27, 62, 70, 78–81]. Recognizing that events leading to acute renal hypoxia are often associated with changes in BVF and/or TVF, and that these changes are accompanied by changes in kidney size, we recently used dynamic MRI to monitor kidney size in parallel with  $T_2^*$ ,  $T_2$  mapping in rats during clinically realistic interventions that alter renal tissue oxygenation. That study demonstrated that monitoring kidney size greatly facilitates the appropriate physiological interpretation of acute renal oxygenation changes obtained by  $T_2^*$ ,  $T_2$  [60]. However, measurements of acute changes in kidney size alone cannot differentiate between changes in the BVF and changes in the TVF. If the reasons underlying a change in kidney size (i.e. changes in TVF or BVF) are not obvious from the respective preclinical or clinical scenario, advanced MR methods that support monitoring of acute changes in BVF and TVF can enable the quantification of their individual contributions to changes in kidney size. MRI-based measurement of renal BVF currently requires off-label administration of intravascular contrast agents, which limits broad use of this approach in patients who may not tolerate such agents [60]. Hence,  $T_2$  assessments of changes in the TVF are highly relevant for elucidating the mechanisms of renal pathophysiology and will help to accurately determine the pathophysiological role of changes in renal oxygenation assessed by renal  $T_2^*$ ,  $T_2$  mapping [80].

The vast majority of reports on  $T_2$  mapping in kidney tissue and its association with kidney injury use a mono-exponential fitting of the  $T_2$  decay [60, 82–85]. Hence, these studies fail to distinguish between the tubular fluid and blood/parenchyma compartments, and incorrectly attribute changes in  $T_2$ . It is standard practice to assume that an MRI voxel consists of homogeneous tissue. However, this is an oversimplification and is especially problematic when imaging renal tissue. A single MRI voxel (the volume element of an image) typically has a size on the order of  $0.25 \times 0.25 \times 1$  mm [3] in preclinical studies. Such a voxel contains at least two, and often all four fluid compartments within renal tissue, including the intracellular space, the interstitial space, the lumen of the intrarenal vasculature with flowing blood, and the tubular lumen with flowing tubular fluid. This results in a multi-exponential  $T_2$  signal decay curve. Therefore, future studies should capitalize on the fact that the  $T_2$  time of water is determined by its varied local environment and use a longer TE range and multi-exponential analysis to gain a more nuanced understanding of  $T_2$  changes associated with renal tissue.

Our results demonstrate that concomitantly measured MRI data on renal TVF, kidney size, and oxygenation-dependent MRI metrics enable assessment of rapid changes in the tubular fluid content, the renal blood content, and kidney size in response to physiological and pharmacological stimuli. Our findings highlight the potential for misinterpretation of data from blood oxygenation level-dependent MRI using  $T_2$  and  $T_2^*$  mapping, and the significant sources of error when using these MRI metrics to estimate tissue oxygenation in the kidney. The increase in TVF upon furosemide administration and the consequent reduction in renal BVF, resulting from compartment syndrome within the rigid capsule of the kidney, mimics an apparent rise in tissue oxygenation as derived from  $T_2$  and  $T_2^*$ . Since these metrics mirror the concentration of

deoxyHb per tissue volume, and because changes in TVF often induce alterations in renal BVF, altered TVF is a prominent cause of changes in  $T_2$ ,  $T_2^*$  that are independent of changes in renal blood oxygenation [62, 80]. Hence, the development, evaluation, and application of methods for TVF measurement are imperative for a correct physiological interpretation of MRI of renal oxygenation.

## 4 | Conclusion

Our study demonstrates the potential of TVF cartography to gain deeper insights into short- and long-term effects of drugs or physiological interventions on the renal TVF and renal oxygenation. MR-based TVF cartography offers a novel approach to investigate the mechanisms of renal disease, and to monitor disease severity and responses to therapy that holds potential promise to ultimately become a clinically impactful noninvasive diagnostic tool.

## 5 | Materials & Methods

All submitted materials and data adhere to the good publishing practices outlined in the Acta Physiologica guidelines for physiology research [86].

### 5.1 | In Vivo Study Preparations

All experiments were approved by the Animal Welfare Department of the State Office of Health and Social Affairs of Berlin, in accordance with German Animal Protection Law and approved guidelines (permission reference is G0043/19). Male Wistar rats ( $n=9$ , aged 12–13 weeks, body mass 270–300 g, Harlan-Winkelmann, Borcheln, Germany) were used. The animals had *ad libitum* access to standard diet and water and were housed under standard conditions with environmental enrichment [60, 63].

Rats underwent surgical procedures involving insertion of vascular catheters and invasive probes for quantitative measurements of renal haemodynamics and oxygenation, as previously described [63]. For anesthesia, urethane (0.2 g/mL in distilled water; 6 mL/kg BM intraperitoneal; Sigma-Aldrich, Steinheim, Germany) was used throughout the surgical preparation and examination [63, 87–90]. Urethane provides long-lasting anesthesia with minimal effects on cardiovascular and respiratory control compared to other anesthetics.

### 5.2 | MRI Protocols

MRI was performed on a 9.4 Tesla small animal MR system (Bruker Biospec 94/20, Bruker Biospin, Ettlingen, Germany) using a linear radiofrequency (RF) volume resonator for transmission. For signal reception, a 4-channel surface RF coil array (Bruker Biospin, Ettlingen, Germany) tailored for rats was deployed [63]. For geometric planning and slice positioning,  $T_2$ -weighted pilot scans were acquired. Local volume selective shimming of the magnetic field homogeneity on a voxel

accommodating the left kidney was conducted using an automatic optimization algorithm based on free induction decay length. For  $T_2^*$  mapping, a multi gradient-echo (MGE) technique (Table 1) was used. For  $T_2$  mapping, two multi spin-echo protocols were employed: (i) Long TE range protocol to enable spectral analysis of the renal  $T_2$  decay acquired in vivo from two rats ( $n=2$ ) at baseline prior to interventions; (ii) Short TE range protocol used for in vivo assessment of  $T_2$  and TVF in rats ( $n=7$ ) during baseline and intervention [31]. For motion compensation,  $T_2$  and  $T_2^*$  mapping were performed using respiratory triggering [63]. Details of the MRI parameters for both  $T_2$  mapping protocols and the  $T_2^*$  protocol are provided in Table 1.

### 5.3 | Diuretic Intervention

The interventional study used the following workflow: a ~10 min baseline period with MR data acquisition, followed by an intravenous bolus of furosemide (5 mg/kg, Ratiopharm, Ulm, Germany) and a 53  $\mu$ L saline chaser (to ensure that the entire furosemide dose entered the circulation), with MR data acquired for  $\sim 10 \pm 2$  min. Subsequently, the balanced electrolyte solution, Ringer's solution (B. Braun, Melsungen, Germany), was infused at a rate of 12 mL/kg for 10 min to replace fluid and electrolyte loss caused by furosemide, with MR data obtained for  $\sim 10 \pm 2$  min. Rats ( $n=7$ ) underwent interleaved  $T_2^*$  mapping and  $T_2$  mapping with short TE range before and after furosemide injection, and during the Ringer's solution infusion.

### 5.4 | Spectral Analysis of the $T_2$ Relaxation of Renal Parenchyma, and Tubular Fluid

To perform spectral analysis of the  $T_2$  relaxation in rat kidney, we acquired spatially resolved  $T_2$  decay curves acquired from rats ( $n=2$ ) during baseline with the long TE range protocol (Multi spin-echo sequence, last echo time TE=292.32 ms, Table 1) For spectral analysis, the data were then analyzed using a free fit with the nonnegative least squares (NNLS) algorithm implemented in the qMRLab module (<https://github.com/qMRLab>) for MATLAB (The MathWorks Inc., Natick, MA, USA) [61, 91, 92]. This was done to specify  $T_{2\_long}$  and  $T_{2\_short}$  range limits of renal tissue. The spectral analysis yields a spectrum of the contributions of all exponential basis vectors to the signal decay. The output is a  $T_2$  coefficient distribution with distinct log-normal-like peaks, where each peak corresponds to (a) major  $T_2$  compartment(s) [93–95]. The spectral analysis was performed without fixing  $T_2$  values or imposing a priori constraints on the number of peaks.

### 5.5 | Decomposition of the $T_2$ Decay to Obtain Tubular Volume Fraction

In healthy rats, parenchyma and blood compartments exhibit similar  $T_2$  relaxation times (9.4 T,  $T_2 \approx 52$  ms in the medulla and a  $T_2 \approx 41$  ms renal cortex,  $T_2 \approx 40$  ms arterial blood), and only the tubular fluid has a considerably longer  $T_2$  relaxation ( $\approx 150 \pm 45$  ms, 37°C,  $n=2$ , pH=6.0) [32, 33]. Based on this and on the outcome of our spectral analysis of the  $T_2$  decay, we used a bi-exponential model of kidney tissue, in which the

long  $T_2$  component is attributed to tubular fluid, while the short  $T_2$  components correspond to parenchymal tissue and blood compartments.

$$I(t) = A_1 \exp(-t/T_{2\_long}) + A_2 \exp(-t/T_{2\_short}) \quad (1)$$

$I(t)$  is the signal amplitude and the evolution time used for  $T_2$ -weighting.  $T_{2\_long}$  and  $T_{2\_short}$  are the  $T_2$  relaxation times of the long and short components;  $A_1$  is the weight corresponding to the tubule water component, and  $A_2$  is the weight corresponding to renal parenchyma and blood.

The fitting was performed using nonlinear regression bi-exponential fit of the  $T_2$  decay using MATLAB functions. This analysis was applied to  $T_2$  decay curves acquired from rats ( $n=7$ ) before and during furosemide intervention using the short TE range protocol (Table 1). For the fitting procedure, the limits for  $T_{2\_short}$  were set to 10–40ms, corresponding to parenchyma and blood components.  $T_{2\_long}$  was fixed at 150ms for tubular fluid. The short TE-range protocol used for TVF assessment in interventional in vivo experiments was designed to balance the constraints of acquisition time, spatial resolution, and signal-to-noise ratio (SNR) [31], however, fixation is necessary since the maximum echo time ( $TE_{max}=83.2$ ms) is suboptimal to estimate  $T_{2\_long}$  range up to 280ms. Fixing some coefficients of the parameters is common practice to increase fit stability and to improve the sensitivity to physiological changes [96]. Mean absolute error (MAE) obtained from our phantom and simulation studies, using the same fixed  $T_{2\_long}$  value, was sufficiently small, as previously demonstrated [31]. To compute the TVF, the ratio of the weight of longer  $T_2$  to the total sum of weights was determined.

$$MAE = \frac{\sum_{n=1}^N |x' - x|}{N} \quad (2)$$

## 5.6 | Validation of TVF Assessment in Phantom Study

To assess absolute TVF values acquired from the bi-exponential decomposition with a fixed  $T_2$  from short TE range protocol, we developed a phantom consisting of two laboratory tubes (0.5mL); one tube containing rat urine, and the other tube containing material mimicking  $T_2/T_1$  relaxation properties of rat renal tissue. For the latter, pure water was doped with a mixture of  $MnCl_2$  and  $CuSO_4$  (Carl Roth GmbH, Karlsruhe, Germany) to mimic the  $T_2$  and  $T_1$  relaxation times characteristic of rat kidney tissue. Each tube was placed in a larger tube (2mL) with distilled water, serving as a reference.

## 5.7 | Simulation of TVF Estimation Error Arising From Fixation of $T_{2\_long}$

Our  $T_2$  measurements in urine provided  $T_2=150 \pm 45$ ms. Because of this bandwidth of  $\pm 45$ ms, we assessed potential errors of TVF estimation induced by fixing  $T_{2\_long}$  to 150ms. For this assessment, we used discrete  $T_2$  values of  $T_{2\_long}(\min)=100$ ms and  $T_{2\_long}(\max)=200$ ms for simulation. This is to demonstrate the impact of a wrong fixation of  $T_{2\_long}=150$ ms on TVF

measurements during the analysis of the short TE range protocol. We simulated the actual  $T_2$  echo modulation curve in a realistic Multi-echo spin-echo (MESE) MRI experiment, using the Bloch-simulation toolkit (<https://web.stanford.edu/~bah/software/epg/>). The simulated  $T_2$  decay could be composed as:

$$S(t) = M_0 \sum_{j=1}^2 (D_j(T_2) \cdot EPG(T_2, \theta^-) dT_2 + \epsilon(0, \sigma n)) \quad (3)$$

where  $S(t)$  is the signal amplitude;  $M_0$  represents the initial magnetization and signal intensity  $TE=0$ , which is equal to the assumed proton density, and  $j=2$ , the number of water compartments.  $D_j$  denotes the amplitude associated with each compartment, and  $j$  is the compartment index. EPG is the output of the extended phase graph algorithm;  $\theta^-$  stands for all other required parameters. The  $\epsilon(0, \sigma n)$  function indicates the additive white Gaussian noise. Gaussian distributed white noise was applied to the signal, such that  $SNR = \text{mean}(s)/\sigma$  is similar to the noise typically found in the magnitude images from in vivo studies. A synthetic dataset of simulated MESE  $T_2$  decay curves, resembling a two-compartment model of kidney tissue, was generated by combining the signal amplitudes of the long component (tubular fluid;  $T_{2\_long}=[100, 150, 200\text{ms}]$ ) with those of the short component (tissue/blood;  $T_{2\_short}=30$ ms) across varying TVF values (ranging from 20% to 80% in 5% increments). The other parameters used in the simulations are similar to the short TE range protocol;  $TR=500$ ms, number of echoes=13, first  $TE=6.4$ ms, inter-echo time  $\Delta TE=6.4$ ms, refocusing flip angle=170° (to account for imperfect refocusing pulses),  $SNR=100$ .

After the simulation, the data sets were fitted using a bi-exponential model with the fixed  $T_{2\_long}=150$ ms for all three ground truths of  $T_{2\_long}=[100, 150, 200\text{ms}]$  to examine what the error of relative changes in TVF is if  $T_{2\_long}$  is fixed to a value below, equal or higher than its true value. Relative changes refer to the difference in a TVF's value between two consecutive time points, expressed as a percentage of the value of the previous time point. It is calculated as:

$$TVF \text{ Relative Change} = \frac{TVF_n - TVF_{n-1}}{TVF_{n-1}} \times 100 \quad (4)$$

where  $TVF_n$  is the value of TVF at time point  $n$ ,  $TVF_{n-1}$  is the value of the TVF at the previous time point,  $n-1$ . To simulate image filtering broadly applied to MRI or averaging over ROIs, the results of nine simulations were averaged to form the final result. The Mean Absolute Error (MAE) as described in Eq. 2 quantifies the discrepancy between  $x'$  (= the TVF relative changes observed from a fitting) and  $x$  (=the actual TVF relative changes),  $x'$  is the estimated result of the  $n^{\text{th}}$  trial, and  $N$  denotes the number of trials ( $N=1000$ ).

## 5.8 | Image Analysis, Data Analysis and Statistics

TVF cartography was performed using a voxel-wise bi-exponential fit of the  $T_2$  decay with  $T_{2\_short}$  constrained between 10ms and 40ms, and  $T_{2\_long}$  fixed at 150ms. Parametric maps of absolute  $T_2^*$  and  $T_2$  were calculated by pixel-wise mono-exponential fitting to the signal intensities of the

$T_2^*$ - and  $T_2$ -weighted images acquired at different echo times [63]. Median  $T_2^*$ ,  $T_2$  and TVF values were calculated for regions-of-interest (ROI) placed in the renal cortex (CO), outer medulla (OM), and inner medulla (IM). ROI positioning was conducted using a standardized semiautomatic approach [97]. This procedure positions the ROIs (5 for CO and OM each, 3 for IM) such that they exclude the transition regions between renal layers to avoid partial volume effects.

For  $T_2$  mapping-based determination of kidney size (KS), segmentation of the coronal mid-slice cross-sectional area of the kidney (here referred to as “kidney size,” KS) was performed using an automatic bean-shaped model [63].

To separate  $T_2^*$  changes unrelated to deoxyhemoglobin from those associated with oxygenation (reflected in  $T_2'$ ),  $T_2'$  was estimated:

$$\frac{1}{T_2^*} = \frac{1}{T_2} + \frac{1}{T_2'} \quad (5)$$

Data were evaluated for Gaussian distribution using the Shapiro–Wilk test. Relative intervention-mediated changes of  $T_2$ ,  $T_2^*$ ,  $T_2'$ , TVF, and kidney size were analyzed using the nonparametric repeated-measures Friedman test, followed by Dunn's post hoc test for multiple comparisons. Correlations between relative changes in TVF, kidney size,  $T_2^*$ ,  $T_2$  and  $T_2'$  were assessed using repeated-measures correlation [64]. Data were analyzed using R v.3.6.3 with the packages “rstatix,” “dunn.test,” and “rmcorr” [98–100].  $p < 0.05$  was considered significant.

## 5.9 | Near-Infrared Spectroscopy Setup Used for the Assessment of Total Hemoglobin Concentration

In order to verify the postulated reduction in BVF after the furosemide bolus, we monitored the hemoglobin concentration per tissue volume in nine healthy rats with an in-house built continuous-wave NIRS setup [101]. Using fiber-optic probes, we acquired the diffuse reflectance of light reemerging from kidney tissue at distances from the laser light source between 1 mm and 8 mm. The probe comprises two independent source fibers and seven detection fibers (Thorlabs Inc., FG200LCC, 200  $\mu$ m core diameter, numerical aperture (NA) 0.27) with a spacing of 1 mm. The diffuse transmittance through the kidney was measured with three additional detection fibers (Thorlabs Inc., FT200UMT, 200  $\mu$ m core diameter, NA 0.39) positioned at the opposite side of the kidney from the two sources. The light of nine lasers (Omicron-Laserage GmbH, LightHub-6 & LightHub-4, 660, 685, 730, 785, 808, 850, 905, 980, and 1060 nm) was used as a source for 4.7 ms each in every acquisition cycle (50 ms). Using a 2  $\times$  2 fiber switch (Leoni GmbH) this light was alternated between the two source fibers after every acquisition cycle. The light was detected with 10 avalanche photodiodes (Hamamatsu Photonics K.K.) equipped with reflective longpass filters, which reject all ambient light below 650 nm. Remaining background light was continuously monitored during the fiber switching time when all lasers were off and was subtracted from all signals.

A GPU-based Monte Carlo simulation [102, 103] of the photon transport through the kidney was used to model the expected signals. The code was modified to produce histograms of the traveled path lengths of the photons in two layers (6 mm thick medulla and 2 mm thick renal cortex on both sides).

In order to reduce the number of open fit parameters, the wavelength dependence of the scattering coefficients was modeled using a power law function. The absorption was modeled as a linear combination of the spectra of oxy- and deoxy-hemoglobin, water, fat, and cytochrome C [104–106]. Since the contribution of fat to the absorption is only very small, its concentration was fixed in the modeling to be half of the nonwater content. The optical properties were extracted from the measured data using a generalized least-squares fit of the database lookup to the data.

The absolute sensitivities of all source-wavelength-detector combinations, their uncertainties and correlations were determined after every in vivo experiment by calibration measurements on 11 distinct epoxy-resin- and PDMS-based tissue phantoms with known absorption and scattering coefficients.

## Author Contributions

E.T.: conceptualization, data curation, formal analysis, investigation, methodology, software, validation, visualization, writing original draft. T.G.: conceptualization, data curation, formal analysis, investigation, methodology, software, validation, supervision, review, and editing. J.M.M.: data curation, formal analysis, software, validation, review, and editing. K.C.: data curation, investigation, methodology, review, and editing. E.S.: conceptualization, methodology, validation, review, and editing. T.N.: conceptualization, funding acquisition, methodology, validation, resources, supervision, review and editing.

## Acknowledgments

This work has been funded in part (TN) by the Deutsche Forschungsgemeinschaft (DFG, German Research Foundation)—project number/Projektnummer, NI 532/27-1. The authors thank A. Anger (Institute of Translational Physiology, Charité–Universitätsmedizin, Berlin, Germany) A. Pohlmann, J.S. Periquito (Max-Delbrueck Center for Molecular Medicine in the Helmholtz Association, Berlin, Germany) and D. Grosenick (Physikalisch-Technische Bundesanstalt, Berlin, Germany) for technical and other support.

## Conflicts of Interest

The authors declare no conflicts of interest.

## Data Availability Statement

The data that support the findings of this study are available on request from the corresponding author. The data are not publicly available due to privacy or ethical restrictions.

## References

1. J. Cao, S. Zhu, M. Ye, et al., “Comparison of Renal Artery vs Renal Artery-Vein Clamping During Partial Nephrectomy: A System Review and Meta-Analysis,” *Journal of Endourology* 34, no. 4 (2020): 523–530.
2. S. O. Schoenberg, S. Aumann, A. Just, et al., “Quantification of Renal Perfusion Abnormalities Using an Intravascular Contrast Agent (Part 2): Results in Animals and Humans With Renal Artery Stenosis,” *Magnetic Resonance in Medicine* 49, no. 2 (2003): 288–298.

3. J. A. Kellum and J. R. Prowle, "Paradigms of Acute Kidney Injury in the Intensive Care Setting," *Nature Reviews. Nephrology* 14, no. 4 (2018): 217–230.
4. M. Haase, R. Bellomo, D. Story, et al., "Effect of Mean Arterial Pressure, Haemoglobin and Blood Transfusion During Cardiopulmonary Bypass on Post-Operative Acute Kidney Injury," *Nephrology, Dialysis, Transplantation* 27, no. 1 (2012): 153–160.
5. L. Li, H. Fu, and Y. Liu, "The Fibrogenic Niche in Kidney Fibrosis: Components and Mechanisms," *Nature Reviews. Nephrology* 18, no. 9 (2022): 545–557.
6. S. J. Chadban and R. C. Atkins, "Glomerulonephritis," *Lancet* 365, no. 9473 (2005): 1797–1806.
7. L. Tonneijck, M. H. Muskiet, M. M. Smits, et al., "Glomerular Hyperfiltration in Diabetes: Mechanisms, Clinical Significance, and Treatment," *Journal of the American Society of Nephrology* 28, no. 4 (2017): 1023–1039.
8. J. van der Weijden, S. V. K. Mahesh, M. van Londen, et al., "Early Increase in Single-Kidney Glomerular Filtration Rate After Living Kidney Donation Predicts Long-Term Kidney Function," *Kidney International* 101, no. 6 (2022): 1251–1259.
9. M. E. Roumelioti, T. S. Ing, H. Rondon-Berrios, et al., "Principles of Quantitative Water and Electrolyte Replacement of Losses From Osmotic Diuresis," *International Urology and Nephrology* 50, no. 7 (2018): 1263–1270.
10. R. C. Blantz, B. J. Tucker, L. Gushwa, and O. W. Peterson, "Mechanism of Diuresis Following Acute Modest Hyperglycemia in the Rat," *American Journal of Physiology. Renal Physiology* 244, no. 2 (1983): F185–F194.
11. X. Huang, E. Dorhout Mees, P. Vos, S. Hamza, and B. Braam, "Everything We Always Wanted to Know About Furosemide but Were Afraid to Ask," *American Journal of Physiology. Renal Physiology* 310, no. 10 (2016): F958–F971.
12. R. Magistroni, C. Corsi, T. Marti, and R. Torra, "A Review of the Imaging Techniques for Measuring Kidney and Cyst Volume in Establishing Autosomal Dominant Polycystic Kidney Disease Progression," *American Journal of Nephrology* 48, no. 1 (2018): 67–78.
13. M. Fähring, E. Seeliger, A. Patzak, and P. B. Persson, "Understanding and Preventing Contrast-Induced Acute Kidney Injury," *Nature Reviews Nephrology* 13, no. 3 (2017): 169–180.
14. T. Tokas, T. R. Herrmann, A. Skolarikos, U. Nagele, and Training and Research in Urological Surgery and Technology (TRUST)-Group, "Pressure Matters: Intrarenal Pressures During Normal and Pathological Conditions, and Impact of Increased Values to Renal Physiology," *World Journal of Urology* 37 (2019): 125–131.
15. R. G. Evans, "Renal Decapsulation to Treat Ischemic Acute Kidney Injury: A New Twist in an Old Tale," *Critical Care Medicine* 46, no. 2 (2018): 332–333.
16. K. J. Chung, J. H. Kim, G. E. Min, et al., "Changing Trends in the Treatment of Nephrolithiasis in the Real World," *Journal of Endourology* 33, no. 3 (2019): 248–253.
17. P. Puri, F. Friedmacher, M. K. Farrugia, S. Sharma, C. Esposito, and T. K. Mattoo, "Primary Vesicoureteral Reflux," *Nature Reviews Disease Primers* 10, no. 1 (2024): 75.
18. S. Naas, M. Schiffer, and J. Schödel, "Hypoxia and Renal Fibrosis," *American Journal of Physiology. Cell Physiology* 325, no. 4 (2023): C999–C1016.
19. E. Porrini, P. Ruggerenti, S. Luis-Lima, et al., "Estimated GFR: Time for a Critical Appraisal," *Nature Reviews. Nephrology* 15, no. 3 (2019): 177–190.
20. A. Mojtahed, M. A. Anderson, and M. S. Gee, "Morphologic Urologic Imaging," *Urologic Clinics of North America* 52, no. 1 (2025): 1–12.
21. R. L. Luciano and G. W. Moeckel, "Update on the Native Kidney Biopsy: Core Curriculum 2019," *American Journal of Kidney Diseases* 73, no. 3 (2019): 404–415.
22. O. Bane, E. Seeliger, E. Cox, et al., "Renal MRI: From Nephron to NMR Signal," *Journal of Magnetic Resonance Imaging* 58, no. 6 (2023): 1660–1679.
23. R. M. Sandoval and B. A. Molitoris, "Intravital Multiphoton Microscopy as a Tool for Studying Renal Physiology and Pathophysiology," *Methods* 128 (2017): 20–32.
24. J. L. Zhang, G. Morrell, H. Rusinek, et al., "New Magnetic Resonance Imaging Methods in Nephrology," *Kidney International* 85, no. 4 (2014): 768–778.
25. B. Ebrahimi, S. C. Textor, and L. O. Lerman, "Renal Relevant Radiology: Renal Functional Magnetic Resonance Imaging," *Journal of the American Society of Nephrology* 9, no. 2 (2014): 395–405.
26. S. T. Francis, N. M. Selby, and M. W. Taal, "Magnetic Resonance Imaging to Evaluate Kidney Structure, Function, and Pathology: Moving Toward Clinical Application," *American Journal of Kidney Diseases* 82, no. 4 (2023): 491–504.
27. T. Niendorf, T. Gladysz, K. Cantow, J. M. Millward, S. Waiczies, and E. Seeliger, "Magnetic Resonance Imaging of Renal Oxygenation," *Nature Reviews. Nephrology* 21 (2025): 483–502.
28. A. L. MacKay and C. Laule, "Magnetic Resonance of Myelin Water: An In Vivo Marker for Myelin," *Brain Plasticity* 2, no. 1 (2016): 71–91.
29. E. Alonso-Ortiz, I. R. Levesque, and G. B. Pike, "MRI-Based Myelin Water Imaging: A Technical Review," *Magnetic Resonance in Medicine* 73, no. 1 (2015): 70–81.
30. W. Sobol and M. Pintar, "NMR Spectroscopy of Heterogeneous Solid-Liquid Mixtures. Spin Grouping and Exchange Analysis of Proton Spin Relaxation in a Tissue," *Magnetic Resonance in Medicine* 4, no. 6 (1987): 537–554.
31. E. Tasbihi, T. Gladysz, J. M. Millward, et al., "In Vivo Monitoring of Renal Tubule Volume Fraction Using Dynamic Parametric MRI," *Magnetic Resonance in Medicine* 91, no. 6 (2024): 2532–2545.
32. A. Pohlmann, J. Hentschel, M. Fechner, et al., "High Temporal Resolution Parametric MRI Monitoring of the Initial Ischemia/Reperfusion Phase in Experimental Acute Kidney Injury," *PLoS One* 8, no. 2 (2013): e57411.
33. S. Yoshimura, H. Tanaka, S. Kawabata, et al., "Effect of Urinary Glucose Concentration and pH on Signal Intensity in Magnetic Resonance Images," *Japanese Journal of Radiology* 40, no. 9 (2022): 930–938.
34. M. Kosaka, N. Owatari, Y. Seo, et al., "In Vivo NMR Micro-Imaging of Kidney and Liver of Mouse at 9.4 T," *Japanese Journal of Physiology* 50, no. 4 (2000): 463–467.
35. S. P. Lee, A. C. Silva, K. Ugurbil, and S. G. Kim, "Diffusion-Weighted Spin-Echo fMRI at 9.4 T: Microvascular/Tissue Contribution to BOLD Signal Changes," *Magnetic Resonance in Medicine* 42, no. 5 (1999): 919–928.
36. W. T. Zhao, K. H. Herrmann, R. Sibgatulin, et al., "Perfusion and T2 Relaxation Time as Predictors of Severity and Outcome in Sepsis-Associated Acute Kidney Injury: A Preclinical MRI Study," *Journal of Magnetic Resonance Imaging* 58 (2023): 1954–1963.
37. B. Haddock, H. B. W. Larsson, S. Francis, and U. B. Andersen, "Human Renal Response to Furosemide: Simultaneous Oxygenation and Perfusion Measurements in Cortex and Medulla," *Acta Physiologica* 227, no. 1 (2019): e13292.
38. M. L. Glociczki, J. F. Glockner, L. O. Lerman, et al., "Preserved Oxygenation Despite Reduced Blood Flow in Poststenotic Kidneys in Human Atherosclerotic Renal Artery Stenosis," *Hypertension* 55, no. 4 (2010): 961–966.

39. M. Pruijm, B. Milani, and M. Burnier, "Blood Oxygenation Level-Dependent MRI to Assess Renal Oxygenation in Renal Diseases: Progresses and Challenges," *Frontiers in Physiology* 7 (2016): 667.
40. H. Lal, P. Singh, K. Ponmalai, et al., "Role of Blood Oxygen Level-Dependent Magnetic Resonance Imaging in Studying Renal Oxygenation Changes in Renal Artery Stenosis," *Abdominal Radiology (NY)* 47, no. 3 (2022): 1112–1123.
41. P. V. Prasad and F. H. Epstein, "Changes in Renal Medullary pO<sub>2</sub> During Water Diuresis as Evaluated by Blood Oxygenation Level-Dependent Magnetic Resonance Imaging: Effects of Aging and Cyclooxygenase Inhibition," *Kidney International* 55, no. 1 (1999): 294–298.
42. R. Wang, Z. Lin, S. Quan, et al., "Evaluation of Renal Tubular Function by Multiparametric Functional MRI in Early Diabetes," *Magnetic Resonance in Medicine* 109 (2024): 100–107.
43. M. L. Glociczki, J. Glockner, S. I. Gomez, et al., "Comparison of 1.5 and 3 T BOLD MR to Study Oxygenation of Kidney Cortex and Medulla in Human Renovascular Disease," *Investigative Radiology* 44, no. 9 (2009): 566–572.
44. J. L. Zhang, G. Morrell, H. Rusinek, et al., "Measurement of Renal Tissue Oxygenation With Blood Oxygen Level-Dependent MRI and Oxygen Transit Modeling," *American Journal of Physiology. Renal Physiology* 306, no. 6 (2014): F579–F587.
45. M. E. Hall, M. V. Rocco, T. M. Morgan, et al., "Chronic Diuretic Therapy Attenuates Renal BOLD Magnetic Resonance Response to an Acute Furosemide Stimulus," *Journal of Cardiovascular Magnetic Resonance* 16 (2014): 1–10.
46. N. H. Holstein-Rathlou and P. P. Leyssac, "TGF-Mediated Oscillations in the Proximal Intratubular Pressure: Differences Between Spontaneously Hypertensive Rats and Wistar-Kyoto Rats," *Acta Physiologica Scandinavica* 126, no. 3 (1986): 333–339.
47. P. P. Leyssac, F. M. Karlsen, and O. Skott, "Dynamics of Intrarenal Pressures and Glomerular Filtration Rate After Acetazolamide," *American Journal of Physiology. Renal Physiology* 261, no. 1 Pt 2 (1991): F169–F178.
48. P. P. Leyssac, F. M. Karlsen, N. H. Holstein-Rathlou, and O. Skott, "On Determinants of Glomerular Filtration Rate After Inhibition of Proximal Tubular Reabsorption," *American Journal of Physiology. Renal Physiology* 266, no. 5 Pt 2 (1994): R1544–R1550.
49. M. Silvennoinen, C. Clingman, X. Golay, R. Kauppinen, and P. C. Van Zijl, "Comparison of the Dependence of Blood R<sub>2</sub> and R on Oxygen Saturation at 1.5 and 4.7 Tesla," *Magnetic Resonance in Medicine* 49, no. 1 (2003): 47–60.
50. M. Brezis, Y. Agmon, and F. H. Epstein, "Determinants of Intrarenal Oxygenation. I. Effects of Diuretics," *American Journal of Physiology. Renal Physiology* 267, no. 6 (1994): F1059–F1062.
51. T. Niendorf, T. Gladysz, K. Cantow, et al., "MRI of Kidney Size Matters," *Magma* 37, no. 4 (2024): 651–669.
52. W. R. Jo, S. H. Kim, K. W. Kim, et al., "Correlations Between Renal Function and the Total Kidney Volume Measured on Imaging for Autosomal Dominant Polycystic Kidney Disease: A Systematic Review and Meta-Analysis," *European Journal of Radiology* 95 (2017): 56–65.
53. J. J. Grantham and V. E. Torres, "The Importance of Total Kidney Volume in Evaluating Progression of Polycystic Kidney Disease," *Nature Reviews. Nephrology* 12, no. 11 (2016): 667–677.
54. R. D. Perrone, M.-S. Mouksassi, K. Romero, et al., "Total Kidney Volume Is a Prognostic Biomarker of Renal Function Decline and Progression to End-Stage Renal Disease in Patients With Autosomal Dominant Polycystic Kidney Disease," *Kidney International Reports* 2, no. 3 (2017): 442–450.
55. US Food and Drug Administration, "Qualification of Biomarker—Total Kidney Volume in Studies for Treatment of Autosomal Dominant Polycystic Kidney Disease Guidance for Industry," (2016), <https://www.fda.gov/regulatory-information/search-fda-guidance-documents/qualification-biomarker-total-kidney-volume-studies-treatment-autosomal-dominant-polycystic-kidney>.
56. J. Buturovic-Ponikvar and A. Visnar-Perovic, "Ultrasonography in Chronic Renal Failure," *European Journal of Radiology* 46, no. 2 (2003): 115–122.
57. C. E. Buchanan, H. Mahmoud, E. F. Cox, et al., "Quantitative Assessment of Renal Structural and Functional Changes in Chronic Kidney Disease Using Multi-Parametric Magnetic Resonance Imaging," *Nephrology, Dialysis, Transplantation* 35, no. 6 (2020): 955–964.
58. K. M. Gooding, C. Lienczewski, M. Papale, et al., "Prognostic Imaging Biomarkers for Diabetic Kidney Disease (iBEAT): Study Protocol," *BMC Nephrology* 21, no. 1 (2020): 242.
59. N. M. Selby, P. J. Blankestijn, P. Boor, et al., "Magnetic Resonance Imaging Biomarkers for Chronic Kidney Disease: A Position Paper From the European Cooperation in Science and Technology Action PARENCHIMA," *Nephrology, Dialysis, Transplantation* 33, no. suppl\_2 (2018): ii4–ii14.
60. K. Cantow, T. Gladysz, J. M. Millward, S. Waiczies, T. Niendorf, and E. Seeliger, "Monitoring Kidney Size to Interpret MRI-Based Assessment of Renal Oxygenation in Acute Pathophysiological Scenarios," *Acta Physiologica* 237, no. 2 (2023): e13868.
61. A. Karakuzu, M. Boudreau, T. Duval, et al., "qMRLab: Quantitative MRI Analysis, Under One Umbrella," *Journal of Open Source Software* 5, no. 53 (2020): 2343.
62. A. Pohlmann, K. Arakelyan, J. Hentschel, et al., "Detailing the Relation Between Renal T2\* and Renal Tissue pO<sub>2</sub> Using an Integrated Approach of Parametric Magnetic Resonance Imaging and Invasive Physiological Measurements," *Investigative Radiology* 49, no. 8 (2014): 547–560.
63. T. Gladysz, J. M. Millward, K. Cantow, et al., "Reliable Kidney Size Determination by Magnetic Resonance Imaging in Pathophysiological Settings," *Acta Physiologica* 233, no. 2 (2021): e13701.
64. J. Z. Bakdash and L. R. Marusich, "Repeated Measures Correlation," *Frontiers in Psychology* 8 (2017): 456.
65. M. E. Edwards, S. Periyannan, D. Anaam, A. V. Gregory, and T. L. Kline, "Automated Total Kidney Volume Measurements in Pre-Clinical Magnetic Resonance Imaging for Resourcing Imaging Data, Annotations, and Source Code," *Kidney International* 99, no. 3 (2021): 763–766.
66. B. O. Erokku, C. E. Anderson, C. A. Flask, and K. M. Dell, "Quantitative Magnetic Resonance Imaging Assessments of Autosomal Recessive Polycystic Kidney Disease Progression and Response to Therapy in an Animal Model," *Pediatric Research* 83, no. 5 (2018): 1067–1074.
67. K. Hueper, B. Hensen, M. Gutberlet, et al., "Kidney Transplantation: Multiparametric Functional Magnetic Resonance Imaging for Assessment of Renal Allograft Pathophysiology in Mice," *Investigative Radiology* 51, no. 1 (2016): 58–65.
68. J. Wen, S. Ringgaard, T. Jørgensen, H. Stødkilde-Jørgensen, J. Djurhuus, and J. Frøkiær, "Long-Term Effects of Partial Unilateral Ureteral Obstruction on Renal Hemodynamics and Morphology in Newborn Rats: A Magnetic Resonance Imaging Study," *Urological Research* 30 (2002): 205–212.
69. K. Jiang, H. Tang, P. K. Mishra, S. I. Macura, and L. O. Lerman, "Measurement of Murine Kidney Functional Biomarkers Using DCE-MRI: A Multi-Slice TRICKS Technique and Semi-Automated Image Processing Algorithm," *Journal of Magnetic Resonance Imaging* 63 (2019): 226–234.
70. R. G. Evans, C. Ince, J. A. Joles, et al., "Haemodynamic Influences on Kidney Oxygenation: Clinical Implications of Integrative Physiology,"

- Clinical and Experimental Pharmacology & Physiology* 40, no. 2 (2013): 106–122.
71. M. Brezis and S. Rosen, “Hypoxia of the Renal Medulla—Its Implications for Disease,” *New England Journal of Medicine* 332, no. 10 (1995): 647–655.
  72. S. Shu, Y. Wang, M. Zheng, et al., “Hypoxia and Hypoxia-Inducible Factors in Kidney Injury and Repair,” *Cells* 8, no. 3 (2019): 207.
  73. M. Hultstrom, M. Becirovic-Agic, and S. Jonsson, “Comparison of Acute Kidney Injury of Different Etiology Reveals In-Common Mechanisms of Tissue Damage,” *Physiological Genomics* 50, no. 3 (2018): 127–141.
  74. S. Ma, R. G. Evans, N. Iguchi, et al., “Sepsis-Induced Acute Kidney Injury: A Disease of the Microcirculation,” *Microcirculation* 26, no. 2 (2019): e12483.
  75. H. Scholz, F. J. Boivin, K. M. Schmidt-Ott, et al., “Kidney Physiology and Susceptibility to Acute Kidney Injury: Implications for Renoprotection,” *Nature Reviews. Nephrology* 17, no. 5 (2021): 335–349.
  76. A. C. Hesp, J. A. Schaub, P. V. Prasad, et al., “The Role of Renal Hypoxia in the Pathogenesis of Diabetic Kidney Disease: A Promising Target for Newer Renoprotective Agents Including SGLT2 Inhibitors?,” *Kidney International* 98, no. 3 (2020): 579–589.
  77. A. M. Jensen, R. Nørregaard, S. O. Topcu, J. Frøkiær, and M. Pedersen, “Oxygen Tension Correlates With Regional Blood Flow in Obstructed Rat Kidney,” *Journal of Experimental Biology* 212, no. 19 (2009): 3156–3163.
  78. L. P. Li, B. Hack, E. Seeliger, and P. V. Prasad, “MRI Mapping of the Blood Oxygenation Sensitive Parameter T(2)\* in the Kidney: Basic Concept,” *Methods in Molecular Biology* 2216 (2021): 171–185.
  79. T. Niendorf, E. Seeliger, K. Cantow, B. Flemming, S. Waiczies, and A. Pohlmann, “Probing Renal Blood Volume With Magnetic Resonance Imaging,” *Acta Physiologica (Oxford)* 228, no. 4 (2020): e13435.
  80. T. Niendorf, A. Pohlmann, K. Arakelyan, et al., “How Bold Is Blood Oxygenation Level-Dependent (BOLD) Magnetic Resonance Imaging of the Kidney? Opportunities, Challenges and Future Directions,” *Acta Physiologica* 213, no. 1 (2015): 19–38.
  81. E. Seeliger, M. Sendeski, C. S. Rihal, and P. B. Persson, “Contrast-Induced Kidney Injury: Mechanisms, Risk Factors, and Prevention,” *European Heart Journal* 33, no. 16 (2012): 2007–2015.
  82. J. Stabinska, J. Piccolo, A. Chhabra, et al., “MRI Detects Tubulointerstitial Changes in Mouse Models of Radiation-Induced Nephropathy,” *Magnetic Resonance in Medicine* 94 (2025): 251–261.
  83. R. Greite, K. Derlin, D. Hartung, et al., “Diffusion Weighted Imaging and T2 Mapping Detect Inflammatory Response in the Renal Tissue During Ischemia Induced Acute Kidney Injury in Different Mouse Strains and Predict Renal Outcome,” *Biomedicine* 9, no. 8 (2021): 1071.
  84. Y. Yuasa and H. Kundel, “Magnetic Resonance Imaging Following Unilateral Occlusion of the Renal Circulation in Rabbits,” *Radiology* 154, no. 1 (1985): 151–156.
  85. Y. Mei, G. Yang, Y. Guo, et al., “Parametric MRI Detects Aristolochic Acid Induced Acute Kidney Injury,” *Tomography* 8, no. 6 (2022): 2902–2914.
  86. B. L. Jensen and P. B. Persson, *Good Publication Practice in Physiology* 2021 (Wiley Online Library, 2022), e13741.
  87. K. Cantow, M. Ladwig-Wiegand, B. Flemming, A. Pohlmann, T. Niendorf, and E. Seeliger, “Monitoring Renal Hemodynamics and Oxygenation by Invasive Probes: Experimental Protocol,” in *Preclinical MRI of the Kidney: Methods and Protocols* (Springer, 2021), 327–347.
  88. D. Grosenick, K. Cantow, K. Arakelyan, H. Wabnitz, B. Flemming, and A. Skälweit, “Detailing Renal Hemodynamics and Oxygenation in Rats by a Combined Near-Infrared Spectroscopy and Invasive Probe Approach,” *Biomedical Optics Express* 6, no. 2 (2015): 309–323.
  89. T. Kaucsar, A. Hosszu, E. Seeliger, H. M. Reimann, and A. Fekete, “Preparation and Monitoring of Small Animals in Renal MRI,” in *Preclinical MRI of the Kidney: Methods and Protocols* (Springer, 2021), 45–55.
  90. E. Seeliger, K. Cantow, K. Arakelyan, M. Ladwig, P. B. Persson, and B. Flemming, “Low-Dose Nitrite Alleviates Early Effects of an X-Ray Contrast Medium on Renal Hemodynamics and Oxygenation in Rats,” *Investigative Radiology* 49, no. 2 (2014): 70–77.
  91. A. Mackay, K. Whittall, J. Adler, D. Li, D. Paty, and D. Graeb, “In Vivo Visualization of Myelin Water in Brain by Magnetic Resonance,” *Magnetic Resonance in Medicine* 31, no. 6 (1994): 673–677.
  92. C. L. Lawson and R. J. Hanson, *Solving Least Squares Problems* (SIAM, 1995).
  93. T. Niendorf, R. M. Dijkhuizen, D. G. Norris, M. van Lookeren Campagne, and K. Nicolay, “Biexponential Diffusion Attenuation in Various States of Brain Tissue: Implications for Diffusion-Weighted Imaging,” *Magnetic Resonance in Medicine* 36, no. 6 (1996): 847–857.
  94. V. Wiggermann, I. Vavasour, S. Kolind, A. L. MacKay, G. Helms, and A. Rauscher, “Non-Negative Least Squares Computation for In Vivo Myelin Mapping Using Simulated Multi-Echo Spin-Echo T2 Decay Data,” *NMR in Biomedicine* 33, no. 12 (2020): e4277.
  95. K. P. Whittall and A. L. MacKay, “Quantitative Interpretation of NMR Relaxation Data,” *Journal of Magnetic Resonance* 84, no. 1 (1989): 134–152.
  96. R. van der Bel, O. J. Gurney-Champion, M. Froeling, E. S. G. Stroes, A. J. Nederveen, and C. T. P. Krediet, “A Tri-Exponential Model for Intravoxel Incoherent Motion Analysis of the Human Kidney: In Silico and During Pharmacological Renal Perfusion Modulation,” *European Journal of Radiology* 91 (2017): 168–174.
  97. L. Riaz, B. Milani, J. S. Periquito, et al., “Subsegmentation of the Kidney in Experimental MR Images Using Morphology-Based Regions-Of-Interest or Multiple-Layer Concentric Objects,” in *Preclinical MRI of the Kidney: Methods and Protocols* (Springer, 2021), 549–564.
  98. A. Kassambara, “Rstatix: Pipe-Friendly Framework for Basic Statistical Tests (R Package Version 0.7.0) [Computer Software],” (2021), <https://cran.r-project.org/web/packages/rstatix/index.html>.
  99. T. Morgan-Wall, “Rayshader: Create Maps and Visualize Data in 2D and 3D,” (2020), <https://tylormorganwall.r-universe.dev/rayshader>.
  100. A. Dinno and M. A. Dinno, “Package ‘dunn.test,’” *Comprehensive R Archive Network Repositories* 10 (2017): 1–7.
  101. T. Gladysz, K. Cantow, B. Flemming, et al., *Towards Depth-Resolved Characterization of Hemodynamics and Oxygenation in the Rat Kidney. European Conference on Biomedical Optics* (Optica Publishing Group, 2019), 11074\_39.
  102. Y. Wang and T. Liu, “Quantitative Susceptibility Mapping (QSM): Decoding MRI Data for a Tissue Magnetic Biomarker,” *Magnetic Resonance in Medicine* 73, no. 1 (2015): 82–101.
  103. E. Alerstam, T. Svensson, and S. Andersson-Engels, “Parallel Computing With Graphics Processing Units for High-Speed Monte Carlo Simulation of Photon Migration,” *Journal of Biomedical Optics* 13, no. 6 (2008): e060504.
  104. S. Kedenburg, M. Vieweg, T. Gissibl, and H. Giessen, “Linear Refractive Index and Absorption Measurements of Nonlinear Optical Liquids in the Visible and Near-Infrared Spectral Region,” *Optical Materials Express* 2, no. 11 (2012): 1588–1611.
  105. R. L. Van Veen, H. J. Sterenborg, A. Pifferi, A. Torricelli, E. Chikoidze, and R. Cubeddu, “Determination of Visible Near-IR Absorption Coefficients of Mammalian Fat Using Time-And Spatially

Resolved Diffuse Reflectance and Transmission Spectroscopy,” *Journal of Biomedical Optics* 10, no. 5 (2005): e054004.

106. O. Bane, I. A. Mendichovszky, B. Milani, et al., “Consensus-Based Technical Recommendations for Clinical Translation of Renal BOLD MRI,” *Magma* 33, no. 1 (2020): 199–215.

### Supporting Information

Additional supporting information can be found online in the Supporting Information section. **Figure S1:** apha70095-sup-0001-FigureS1.docx.